ROBOTICS AND MECHATRONICS

NOVEL DESIGN OF MR-COMPATIBLE PNEUMATIC SOFT-SURGICAL ENDOSCOPE FOR MIS APPLICATIONS WITH VARIABLE STIFFNESS

N. (Nehal) Mathur

MSC ASSIGNMENT

Committee:
dr. ir. J.F. Broenink
Y.X. Mak, MSc
dr. ir. M. Abayazid
dr. ir. H. Naghibi Beidokhti
dr. A. Sadeghi

December, 2020

054RaM2020
Robotics and Mechatronics
EEMCS
University of Twente
P.O. Box 217
7500 AE Enschede
The Netherlands

UNIVERSITY OF TWENTE. | TECHMED CENTRE
UNIVERSITY OF TWENTE. | DIGITAL SOCIETY INSTITUTE

Summary

This study introduces a novel MR-compatible soft-surgical pneumatic endoscope design with variable stiffness for minimally invasive surgeries. The design aims to improve the bending performance of the soft endoscope by shifting the start-up transient out of the operating range, which is at near-straight configuration. Additionally, functionality has been improved by implementing laminar jamming as a variable stiffening mechanism and scalability of modules has been increased. The endoscope design has been based on a study that determines design parameters that influence the performance of the endoscope using Finite Element Method, and the effectiveness of laminar jamming has been estimated analytically. Motion and stiffness characterisation experiments have been performed using the fabricated prototype, testing the bending performance and stiffness in the transverse and axial direction. By modifying the design of the shell-reinforced soft pneumatic actuator, an endoscope with a 12 mm diameter has been designed to be at an angle of 120° at rest, thereby shifting the start-up behaviour out of the operating range, which is at near-straight configuration. A singular actuation chamber improves the scalability of the module. Simulation results indicate that the larger cross-sectional area of the actuation chamber, larger number of rings and smaller backbone width improve the bending range of the endoscope. The analytical model indicates that the stiffness of the jamming structure is dependent on the number of layers, however, based on spatial constraints, five laminar sheets were implemented. The experimental results show an improved bending performance of the endoscope compared to previous work with a successful shift of the start-up behaviour. The variable stiffening mechanism has been shown to increase the stiffness of the endoscope, however, it limits the bending range. Further research is required to develop the designed endoscope for clinical application.

Acknowledgement

This past year would have been unimaginably difficult had I not had the support and encouragement from the Medical Robotics RaM group, the technicians at RaM and from my family and friends.

As my daily supervisor, Yoeko Mak continuously supported and guided me throughout my thesis. I want to thank him for supporting me throughout and asking the difficult questions. My thanks also go to Hamid Naghibi Beidokhti for guiding me through the FE modelling process and without whom I would not have learnt as much as I have. Finally, I would like to thank Momen Abayazid for the opportunity to conduct this research.

Throughout the partial lock-down, due to the Covid-19 pandemic, I had the incredible support of the technicians at RaM who worked tirelessly to help me during the fabrication and experimentation process. Thank you Sander Smits for advising me through the 3D printing process. Thank you Henny Kuipers for helping me with the fabrication of my endoscope and thank you Gerben Te Riet O/G Scholten for taken the time to discuss the progress of my work and brainstorming areas of improvements.

I would like to thank my friends and family, both here and in India, for their endless support and encouragement and I would especially like to thank Kasper Hendriks for his unfailing support throughout.

Contents

1 Introduction

The general trend observed in medicine regarding abdominal surgeries is the increased preference for Minimally Invasive Surgery (MIS). There are several types of minimally invasive surgeries ranging from Multiple-Incision MIS to Single-Incision Lapro-endoscopic Surgeries (SILS), Natural Orifice Transluminal Endoscopic Surgeries (NOTES), Video-Assisted Thoracoscopic Surgery (VATS) and Robotic Surgeries. Compared to Open Surgery (OS), which requires a single but very large incision, MIS requires single or multiple small incisions located close to the surgical target that are large enough to insert surgical tools. Advantages range from drastically reducing patient recovery time to quicker oral intake, reduced pain, lower blood loss, improved cosmetic results and briefer hospitalisation (Robinson and Stiegmann, 2004; Antoniou et al., 2015). Several, if not all minimally invasive surgeries require the use of endoscopes for visual feedback and surgical intervention.

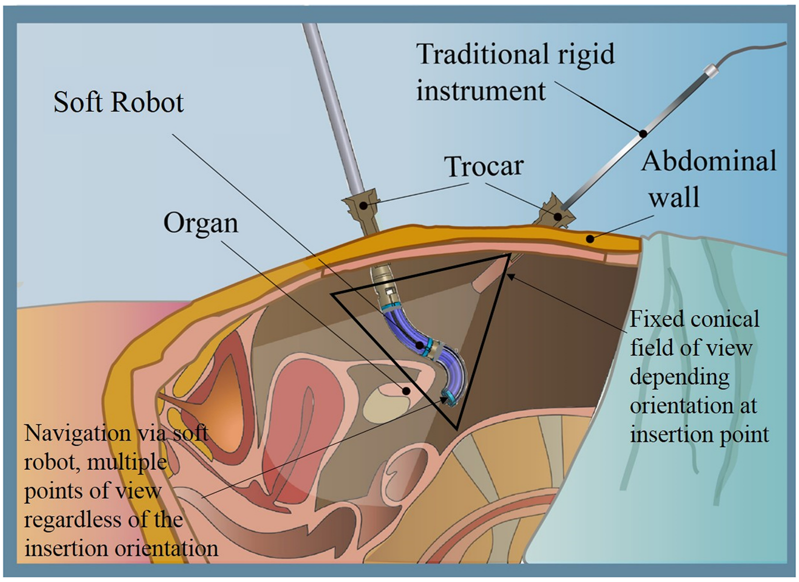

Figure 1.1: A representation of the application of flexible endoscopes when operating on organs or difficult to reach surgical targets. Flexible endoscopes are frequently used for the visualisation of the gastrointestinal tract. The endoscope depicted here is the STIFF-FLOP developed by Abidi et al. (2017).

The primary function of endoscopes is to provide light and visual feedback since MIS removes the surgeon's ability to physically see the surgical target. Recent advances have been made in the robotised steering and development of flexible endoscopes that enable complex surgical intervention (Karimyan et al., 2009; Reilink, 2013; Yeung and Gourlay, 2012). Endoscopes consist of three main parts: the tip, the insertion tube and the control section (Kohli and Baillie, 2019). The distal end, or the tip, of the endoscope houses a camera, water-jet to clean debris off the camera lens, light source and free lumen, which can be used for inserting biopsy forceps. Based on the requirements of the surgery, the tools at the distal end vary.

There are two types of endoscopes; rigid and flexible, where the latter enables the bending of the distal tip and/or the entire device. The flexible endoscope is commonly used for the visualisation of the gastrointestinal (GI) tract (gastroscopes, colonoscopes, esophagogastroduodenoscopy), while rigid endoscopes are used for the visualisation of the abdomen (laparoscope), brain (neuroendoscope) and joints (arthroscope) (Schneider and Feussner, 2017; Runciman et al., 2019). Recent developments have been made to the design of laparoscopes and neuroendoscopes to make them flexible thereby increasing their functionality.

1.1 Shortcomings of Current Developments

Although MIS is advantageous for patients, surgeons have several difficulties manoeuvring instruments within the constricting and sensitive environment of the body. Challenges such as limited motion, uncontrollable stiffness, difficulty tracking the endoscope and overall stability and motion control are common. In general, rigid endoscopes have limited motion and are unable to reach surgical targets that are not within the conical workspace of which the apex is at the point of incision (Abidi et al., 2017).

Flexible endoscopes on the other hand are not limited by their workspace but can have difficulty varying stiffness, which is required for surgical intervention and tracking the endoscope (Kurniawan and Keuchel, 2017; Cianchetti and Menciassi, 2017). Advancements have been made in several of these fields, with STIFF-FLOP, titled “Stiffness-Controllable Flexible and Learnable Manipulator for Surgical Operation”, at the forefront, discussed in further detail in Chapter 2. A miniaturised and modified design based on the STIFF-FLOP, developed by Lin (2019), has a distal outer diameter of 11.5 mm with a central free lumen of diameter 4.5 mm. Three pneumatic actuation chambers are located radially, equidistant and symmetrically, for omnidirectional 2 DOF bending. Radial expansion is limited by the addition of a braided sheath on the outside of the endoscope. One of the advantages of both the STIFF-FLOP and Lin’s endoscope is that they are MRI-compatible which broadens the scope of their applications and enables localisation within an MRI bore.

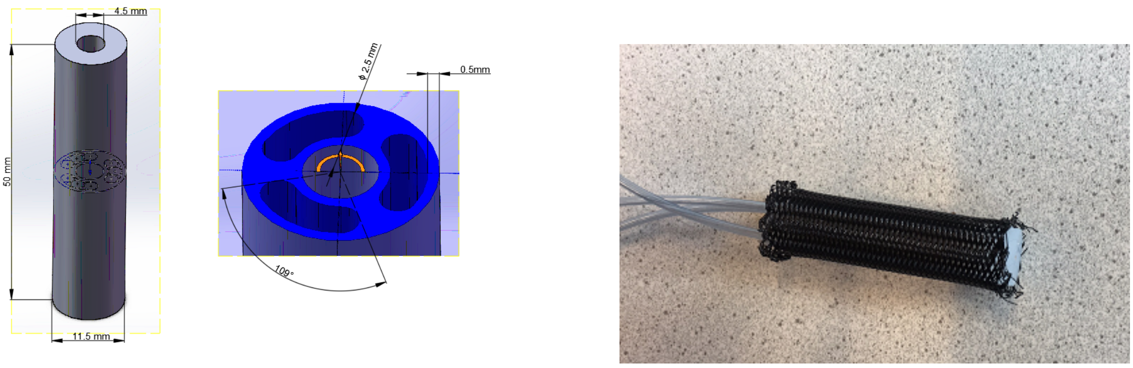

(a) **(b)**

Figure 1.2: The soft endoscope design based on the STIFF-FLOP developed by Lin (2019). Shown in (a) is the 3D CAD model depicting the free central lumen and symmetric pneumatic actuation chambers. Shown in (b) is the complete fabricated piece with outer sheathing to limit radial expansion.

Laparoscopes come in various sizes ranging from 3 mm to 12 mm mm in diameter (Popa et al., 2018). The smallest distal outer diameter of the STIFF-FLOP is 14.5 mm, which is larger than the acceptable maximum of 12 mm. On the other hand, Lin’s design has a distal outer diameter of 11.5 mm and is suitable for laparoscopy. The endoscope can bend 90° with one-plane actuation for an applied input pressure of 0.38 bar. Limitations with the design include a dead zone and non-linear behaviour for small angles making it very difficult to operate at angles smaller than 15°, as is depicted in Figure 1.3a. Reason for the dead zone is the free space between the elastomer and the inner diameter of the external sheathing. Additionally, static friction due to the external sheathing also prevents the initial bending of the endoscope until the chamber is pressurized enough to overcome it. It is difficult to identify which of the two properties has a larger contribution to the dead zone. In Figure 1.3a the dead zone is present up to 0.1 bar.

Another limitation of the design is the hysteresis while bending, depicted in Figure 1.3b. This is the uniaxial hysteresis of Eco-Flex 00-50 becoming prominent for strains higher than 0.20 (Hsu et al., 2013). With inflated chambers, the strain is measured to be between 0.25 to 0.45, which is much larger than 0.20.

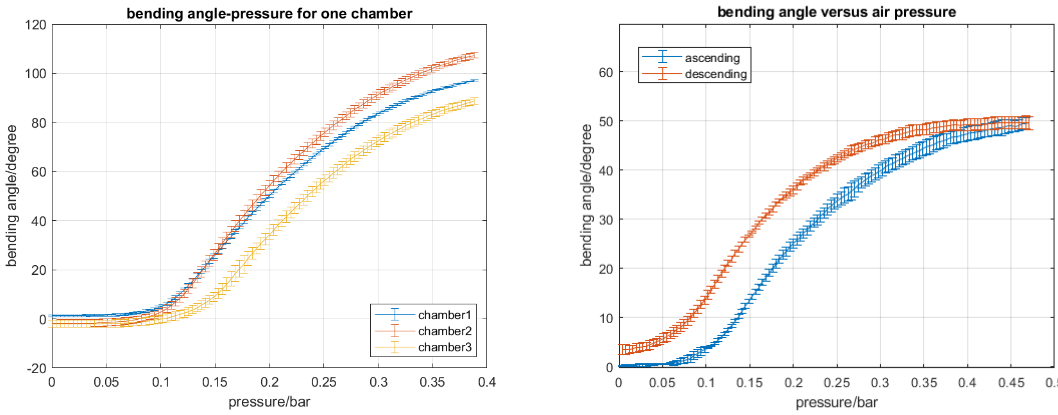

(a) (b)

Figure 1.3: Experimental results of the endoscope designed by Lin (2019). The bending performance of the endoscope with respect to input pressure for (a) single chamber bending, and (b) hysteresis between ascending and descending pressure.

Finally, the endoscope is missing variable stiffening mechanisms required to add rigidity during medical interventions such as when applying force during punctures, biopsies or grasping tasks (Blanc et al., 2017). Variable stiffening mechanisms used in flexible endoscopes are of three types: bulk locking (popular example is granular jamming), segment locking and longitudinal locking (popular example is laminar jamming). Each of these is further explained in Chapter 2. In this study, laminar jamming is used as the variable stiffening mechanism.

The endoscope's inability to operate at small angles due to the presence of a dead-zone, non-linearity and the hysteresis make it difficult to control. Further more, with a three chamber actuation mechanism, the scalability of the modular design is limited, requiring additional space for routing pneumatic tubes when modules are stacked. Therefore, the design proposed in this report works on eliminating these issues while improving scalability and implementing laminar jamming as the variable stiffening mechanism.

1.2 Research Question

The aim of this thesis is to design a flexible soft-surgical endoscope applicable for MIS, specifically laparoscopic surgeries. The research question is therefore formulated as:

"How can an MRI-compatible miniaturized flexible soft-surgical endoscope be designed such that each module's bending performance, stiffness and applied force is within the limits of laparoscopy?".

To answer this research question, certain design goals and research objectives are outlined:

1. Design goals
   (a) Shift dead zone such that the bending performance in the operating range, which is at near-straight configuration, is within the limits of laparoscopy
   (b) Improve space allocation for scalability of the endoscope
2. Research objectives
   (a) To identify design parameters that influence the bending performance of the endoscope
   (b) To identify how effective laminar jamming is as a variable stiffening mechanism.

1.3 Approach

The thesis is a combination of design goals with research objectives, thus a combination of design and scientific approach is used. This consists of an iterative design process where the design requirements are derived from the design goals and models of the two important mechanisms, actuation and stiffening, are used in the development of the novel endoscope design. Additionally, literature is studied and state-of-the-art endoscope designs are reviewed. The performance is then analysed by means of experiments. This approach is depicted in Figure 1.4.

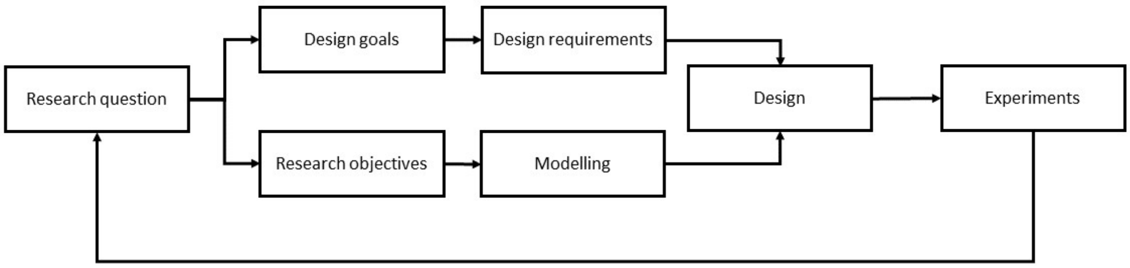

Figure 1.4: Approach taken within this research to answer the research question.

As can be seen in Figure 1.4, the design goals are implemented into the design requirements. The goal of improving the bending performance of the endoscope by shifting the dead zone is considered a design requirement since the dead zone is a product of the pneumatic actuation method designed in combination with an external sheathing. Therefore, to shift the dead zone out of the operating range, which is at near-straight configuration, the endoscope at rest is in a pre-bent position. The second design goal focuses on the scalability of the module. This entails reducing the number of pneumatic chambers thereby decreasing the number of pneumatic tubes required.

The research objectives are met using a combination of modelling and experimentation. The design parameters that influence the bending performance of the endoscope are determined by performing a design study using Finite Element Method (FEM). Additionally, the design parameters that influence the stiffness of the variable stiffening mechanism can be determined with the help of an analytical model. In combination with the design requirements, the final endoscope design is determined, fabricated and tested. The effectiveness of the variable stiffening mechanism is experimentally determined.

1.4 Report Outline

In this report a novel miniaturised flexible soft-surgical endoscope is developed. In Chapter 2, a literature study is performed, analysing the various soft actuators, variable stiffening mechanisms and state-of-the-art endoscopes used in practice, and those currently being developed. The preliminary novel design, based on the design requirements, is explained in Chapter 3. Models of both the actuation and stiffening mechanisms, using FEM and analytical modelling, are created and a final design based on the design study is determined. The fabrication process is discussed in Chapter 4. The endoscopes performance is tested and the results are shown in Chapter 5. Finally, in Chapter 6, the research is discussed and concluded with recommendations for further research.

2 Literature Review

2.1 Introduction

MIS, specifically Laparoscopic Surgery (LS), is performed by creating small incision(s) close to the surgical target through which medical instruments are inserted with the help of trocars, which act as fulcrums for the manoeuvrability of rigid instruments (Abidi et al., 2017). The number and size of incisions vary depending on the surgery performed. An increased interest in MIS has required development and improvement in the functionality of the endoscopes to be able to perform complex tasks, such as surgical intervention or the ability to perform SILS (Runciman et al., 2019).

Currently used endoscopes are of two types; rigid and flexible. Rigid endoscopes are used when the surgical target is close to the incision point since they have limited motion with 4 DOF and an inability of manoeuvring around healthy organs to reach a difficult surgical target (Abidi et al., 2017). Their fixed stiffness enables surgeons to perform surgical tasks and their rigidity maintains their shape making them easier to track. Rigid endoscopes also suffer from instability due to the fulcrum effect which is when the point of insertion acts as the point of rotation that inverts the surgeons movements and amplifies tremors (Runciman et al., 2019). On the other hand, flexible endoscopes have the required manoeuvrability but lack the adjustable stiffness necessary to perform the surgery (Kurniawan and Keuchel, 2017). Another issue with flexible endoscopes is localization since it is difficult to track internally, as the camera's lack of depth perception and horizon stability provides insufficient information to determine the position of the distal tip or rest of the insertion tube (Atallah et al., 2015; Xin et al., 2006). Therefore, advancements are being made in the development of trackable flexible endoscopes with improved manoeuvrability and surgical functionality.

Flexible endoscopes can be constructed with rigid sections that have flexural parts enabling the bending of the distal tip and the body of the endoscope (such as tendon-driven endoscope (Kohli and Baillie, 2019; Cheng et al., 2018)), or are made of flexible material entirely that can bend and is squeezable (Cianchetti et al., 2013). Several state-of-the-art flexible endoscopes in the market today have flexure designs actuated with tendons attached to motors (Kohli and Baillie, 2019).

Soft-endoscopes are a rapidly growing field of study that develops flexible endoscopes using soft-robotics. It is inspired by nature and uses flexible and compliant material in the design and actuation of robotic systems (Kim et al., 2013). Its flexibility and compliance makes it ideal for an endoscope that is required to bend and deform and be inserted deeply without damaging its surroundings (Rus and Tolley, 2015). Depending on the manufacturing, soft robotics enables controllable variable stiffness which facilitates stiffness change of specific parts of the endoscope required for surgery (Manti et al., 2016).

An intrinsic benefit of soft-robotics is its inherent MRI-compatibility. Operating within an MR enables the localisation of the endoscope which is otherwise difficult (Polygerinos et al., 2017). This eliminates the need for a camera or position tracking of the distal end. MRI-compatibility, however, adds complications to the design and control due to the inability of there being any metal within the confines of the room. Therefore, the pneumatic, hydraulic or tendon actuation methods used can result in severe delays.

This chapter provides an overview of soft robotic endoscopes using MR-compatible actuation with an analysis of their advantages and disadvantages. First, MR-compatible soft actuators and stiffening mechanisms currently developed will be discussed. Next, state-of-the-art flexible endoscopes currently used and those being developed will also be reviewed. Among them are the Invndoscope, NeoGuide, endoscopes produced by Olympus, Minimally Invasive

Neurosurgical Intracranial Robot (MINIR), STIFF-FLOP and the Multi-Level Stiffness Controllable (MOLLUSC) endoscope.

2.2 MR Compatible Actuators

There are several MR-compatible actuators used in soft robotics, some of which are outlined below:

Cable Actuators: enable motion of a device by contracting or extending an inextensible cable attached rigidly to the device. An example of this can be seen in Figure 2.1a. It replicates the tendons in the human body and is seen repeatedly in continuum robots (Gifari et al., 2019). This pulling force can be induced using a motor winding and unwinding the cable. The use of a motor is difficult in an MR-environment, with the controls and motors located outside the MR-safe zone. Additional friction and inconvenient wire management make its implementation within the MR bore difficult.

Shape Memory Alloy (SMA): is a smart material that can alter its stiffness and deform when there is a temperature change. The SMA constitutes of nickel titanium (NiTi) alloy wires which contract when heated and relax when cooled, which is particularly useful when generating pulling force (Cheng et al., 2018; Gifari et al., 2019). An example of this can be seen in Figure 2.1b.

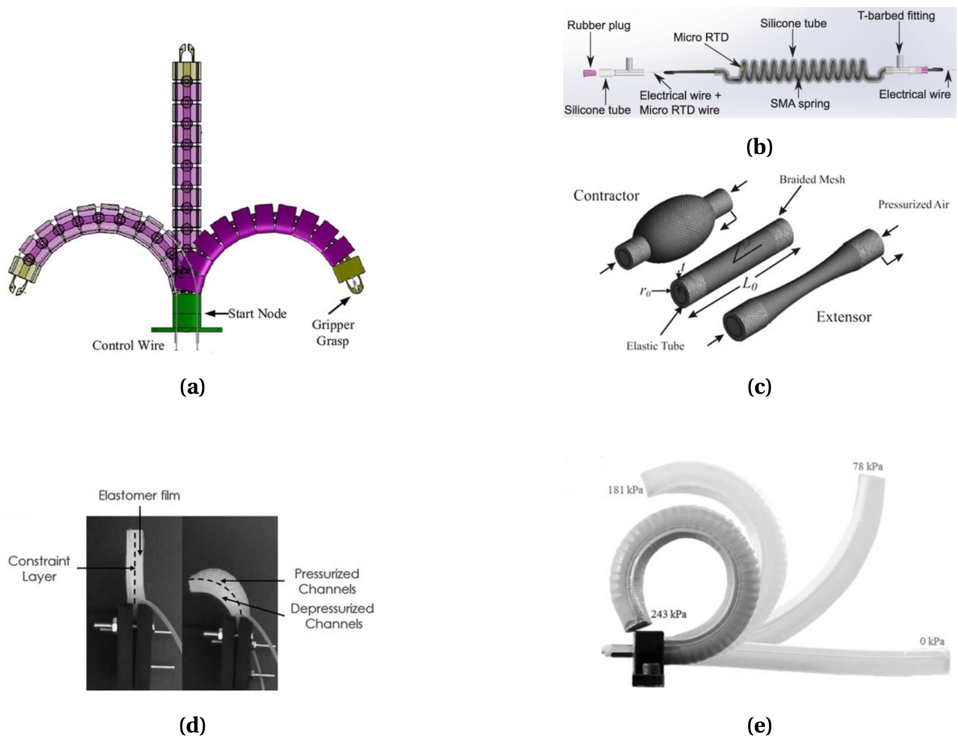

Figure 2.1: Soft actuators that are MRI-compatible: (a) Cable actuators (Li et al., 2011), (b) Shape Memory Alloy (SMA) (Cheng et al., 2017), (c) Pneumatic Artificial Muscle (PAM) (McMahan et al., 2006), (d) Fluidic Elastomer Actuator (FEA) (Marchese et al., 2015) and (e) Fiber-Reinforced FEA (Marchese et al., 2015).

Pneumatic Artificial Muscle (PAM): Soft Pneumatic Actuator (SPA) is another MRI safe medium of actuation which uses fluidic pressure to deform. PAM or McKibben actuators are designed to contract when air pressure is applied. An elastic tube encased in a braided sleeve mesh expands radially and contracts in the axial direction when air pressure is applied. The braided sleeve mesh controls the amount of radial expansion and thus the amount of contraction. Therefore, this actuator applies pulling force, depicted in Figure 2.1c. Based on the deign of the braided sleeve, the actuator can contract, expand and even stiffen (Chou and Hannaford, 1996; Marchese et al., 2015).

Fluidic Elastomer Actuator (FEA): are actuators consisting of two layer of elastic material separated by an inextensible layer that consists of paper, cloth, plastics or a relatively inextensible elastomer which enables primitive motion such as extending, bending and twisting. One of the layers consists of chambers connected through air-channels, which, when pressurized, expand producing localized strain. The combination of the expansion and the inextensible layer results in the actuator motion. Another name for this design is Pneumatic Networks of Pneu-Nets actuators and an example of this can be seen in Figure 2.1d. Another types of FEA is a Fibre-reinforced FEA, where instead of an inextensible layer, an inextensible fibre is wound around an elastomer tube in various designs and angles to enable extension, bending and twisting (Bishop-moser et al., 2012; Marchese et al., 2015). This is depicted in Figure 2.1e.

Shell-Reinforced (SPA): is a novel actuator developed as a design improvement over the unconstrained classical actuators that experienced mechanical failure due to excessive inflation at high pressure inputs. It comprises of two parts: an extremely stretchable single chamber actuator core and an inextensible but bendable shell encasing the former. The shell is used to guide the trajectory of the actuator and constrains excessive ballooning (radial expansion). There are two main types of single chamber shell-reinforced actuators: linear and bending. These are depicted in Figure 2.2. The main difference between the two is the shell pattern. The configuration of the shell, the number of slits and the width of the slits largely influences the performance of the actuator. For the bending SPA, the shell inhibits the extension of the endoscope and in turn, when actuated, bends in the direction of the force applied to the backbone. The slits create rings around the SPA and are connected with a backbone depicted in Figure 2.2 along the inner arc of the bending SPA.

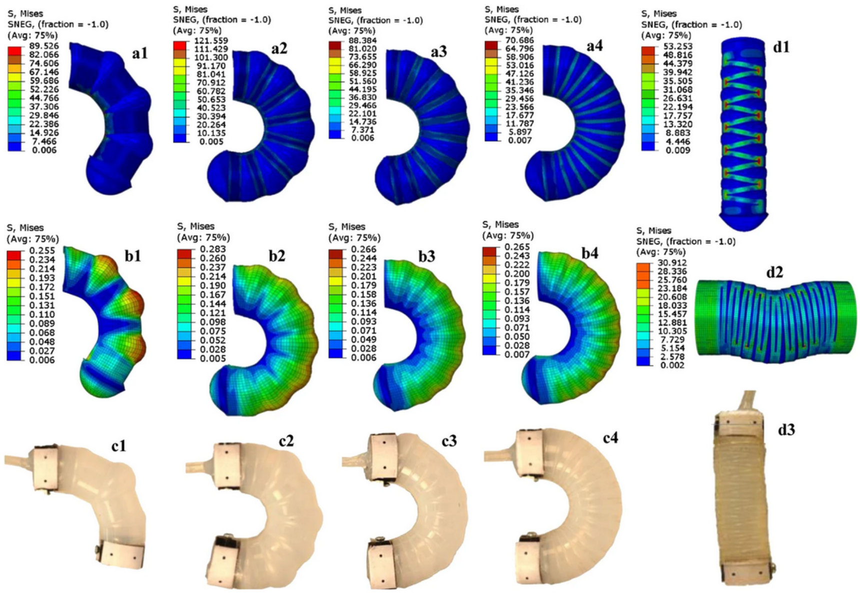

Figure 2.2: Single chamber shell-reinforced SPA with varying number of rings. Figures a1-a4 depict the Von Mises stress of the contour plots of the entire actuator, while figures b1-b4 depict the actuator core alone. Figures c1-c4 depict the fabricated results and figures d1-d3 depict the Von Mises stress contour plots of the linear actuator and the fabricated result (Agarwal et al., 2016).

2.3 MR Compatible Variable Stiffness Mechanisms

As is explained by Blanc et al. (2017), several of the stiffening mechanism found in endoscopic designs that are MR-compatible are primarily based on changing the elastic property of the endoscope using structural interactions. The state-of-the-art stiffening mechanisms that use structural interactions have been outlined below:

Bulk Locking: is a mechanism where a change in stiffness is obtained by modifying the interaction between several elements within a given volume. Granular jamming, a form of bulk locking, for example, induces stiffening using granules embedded within a membrane. By applying a pressure difference, the interactions between the granules and the membrane changes the stiffness of the system. At low pressure difference, the grains are free to move with respect to each other, making the system flexible. At high pressure difference, the grains start to lock with each other, making the system rigid. Examples of granular jamming used in soft robotic systems can be seen in Figure 2.3.

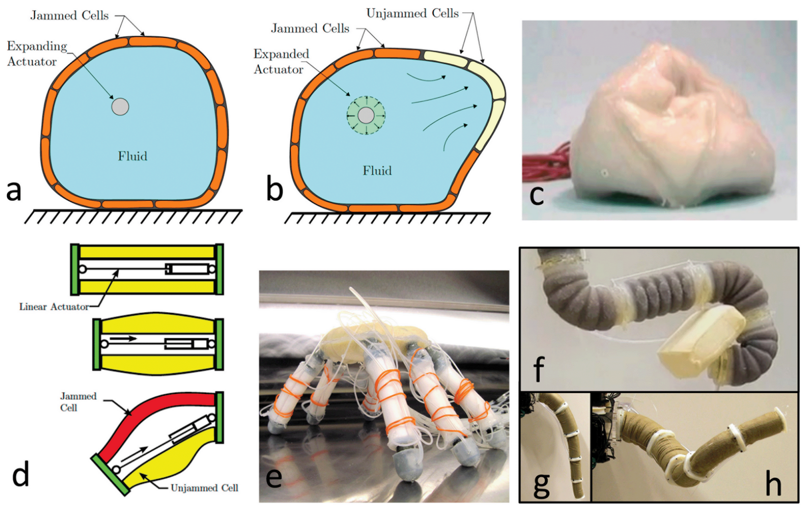

Figure 2.3: Jamming-based soft robotic systems reviewed by (Jaeger, 2015). (a and b) Cross-sectional sketch of JamBot operation. (c) JamBot in contracted state (evacuated interior). (d) Combination of linear actuator and jamming cells to add bending motion. (e) Soft hexapod robot using one linear actuator plus four jamming cells as in (d) for each leg. (f–h) Highly articulated manipulator, picking up a brick (f), unjammed (g), and jammed in corkscrew configuration (h).

Segment Locking: uses a mechanism where the system is divided into several segments with each segment consisting of one element. The segments can consist of various elements, such as cylindrical or spherical joints. Variation in stiffness occurs by modifying the interaction between segments where the principle stimulus is the tension of longitudinal cables used to connect segments. This tension results in friction between the elements thereby inducing stiffness. There are different types of connectors: several wires, a central wire, bellows-like connectors or a soft layer connection. The bellows-like segment connector enables stiffening by locking the segment in a specific angle while the soft layer connection, in combination with wires increases the stiffness of the system when compressed. Examples of these stiffening mechanisms can be found in Figure 2.4.

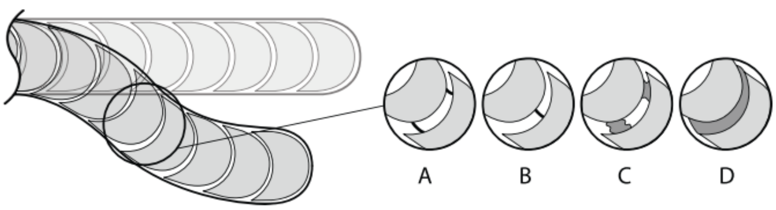

Figure 2.4: Segment locking mechanism composed of structures that can be locked by several inter-segment element using (A) multiple tensioned wires, (B) single central tensioned wire, (C) bellows-like connection and (D) soft material layer (Blanc et al., 2017)

Longitudinal Locking: is a mechanism similar to bulk locking however uses interactions that are longitudinal with respect to the structure. Lamming jamming, for example, creates a variation in stiffness when the interaction between the longitudinal elements, such as thin plates, in changed using pressure difference. The stiffness increases when a pressure difference induces a low or no relative motion between the plates therefore locking the system due to friction. The stiffness induced is heavily dependent on the number of layers and friction between layers. Examples of the use of laminar jamming in soft robotics can be seen in Figure 2.5.

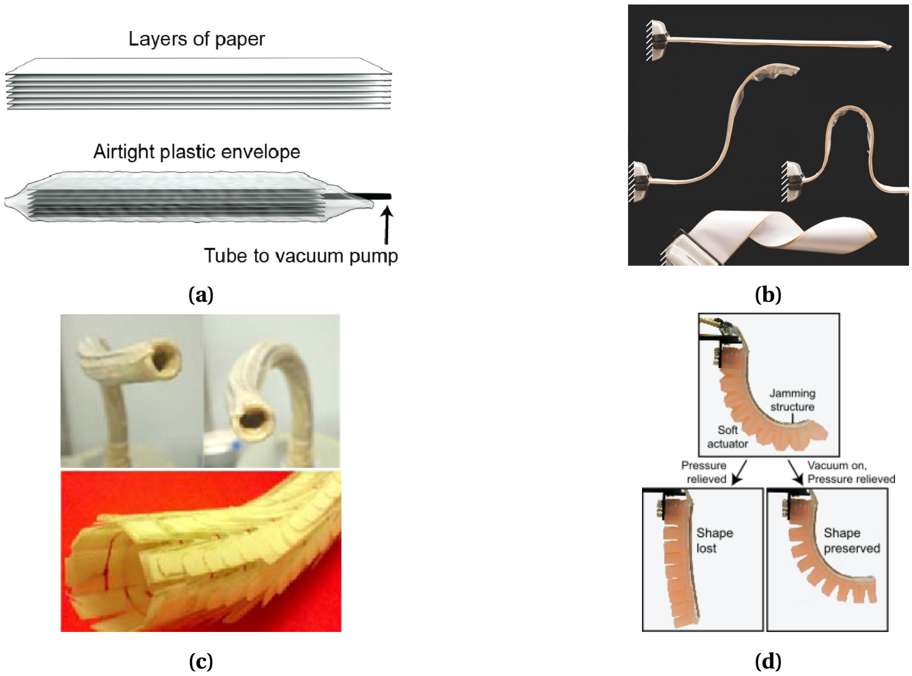

Figure 2.5: Various examples of laminar jamming are depicted here. (a) depicts the basic structure of laminar jamming (Narang et al., 2018) while (b) shows the capabilities of laminar jamming when stiffening is activated (Narang et al., 2018). Application are (c) novel snake scales laminar jamming mechanism for tunable MIS (Kim et al., 2013) and (d) soft grippers (Narang et al., 2018).

2.3.1 Comparison

From the three stiffening mechanisms outlined above, a comparison will be made between granular jamming and laminar jamming based on the reviews by Blanc et al. (2017) and Clark and Rojas (2019). Segment locking is not considered since the design of a miniaturised stiffening mechanism is out of the scope of this assignment. In the review by Blanc et al. (2017), the designs are compared based on their flexural stiffness and activation time while in the review by Clark and Rojas (2019) they were compared based on force resistance and position accuracy. Flexural stiffness is the ability of a structure to resist bending, the activation time measures the speed with which the stiffness changes, the force resistance is a measure of their stiffness and ability to resist external load and finally, the position accuracy is the accuracy of the position after the stiffening mechanism has been activated. Additional factors that will be used to compare the two are hysteresis and safety (Clark and Rojas, 2019). The comparison between two mechanisms is shown in Table 2.1.

In the review by Blanc et al. (2017), the flexural stiffness ranges from the stiffest endoscopes, with 10^7 Nmm^2 bending stiffness, found in market to the the stiffest pediatric endoscopes, with 10^2 Nmm^2 bending stiffness. Endoscopes using granular jamming ranged from the softest endoscopes to the stiffest endoscopes while those using laminar jamming, of which there are limited examples, are only on either end, that is, the softest pediatric endoscope or the stiffest endoscopes. Therefore, endoscopes with different flexural stiffness can be produced using either. Granular jamming has the fastest activation time, lower than 1 s.

In the review by Clark and Rojas (2019), the force resistance of the endoscopes with laminar jamming is better than those with granular jamming. On the other hand, the position accuracy of endoscopes with laminar jamming is poorer. Clark and Rojas (2019) also state that the hysteresis seen with rigid granules is higher compared to all designs.

Finally, in case of rupture or damage to the endoscope, granular jamming is potentially more dangerous as the granules can spread and contaminate the surgical site while laminar jamming is more contained.

Table 2.1: Comparison between granular jamming and laminar jamming based on reviews by Blanc et al. (2017) and Clark and Rojas (2019).

Stiffening Mechanism	Flexural Stiffness	Activation	Force Resistance	Position Accuracy	Hysteresis	Safety
Granular Jamming	+	+	-	+	-	-
Laminar Jamming	+	-	+	-	+	+

2.4 MRI Compatible Endoscopes

Endoscopes found in literature that are MR-compatible in their design are discussed in this section. This includes, tendon-driven endoscopes like MINIR, the STIFF-FLOP, MOLLUSC.

2.4.1 Tendon-Driven Endoscope

Tendon driven continuum robotic endoscope is a flexure designed endoscope with cable actuators that are routed along the length of the device. When a pulling force is applied by winding the cable/tendon length, the device is forced to bend. Several advancements have been made in the production and design of tendon-driven endoscopes where MINIR is a noticeable example.

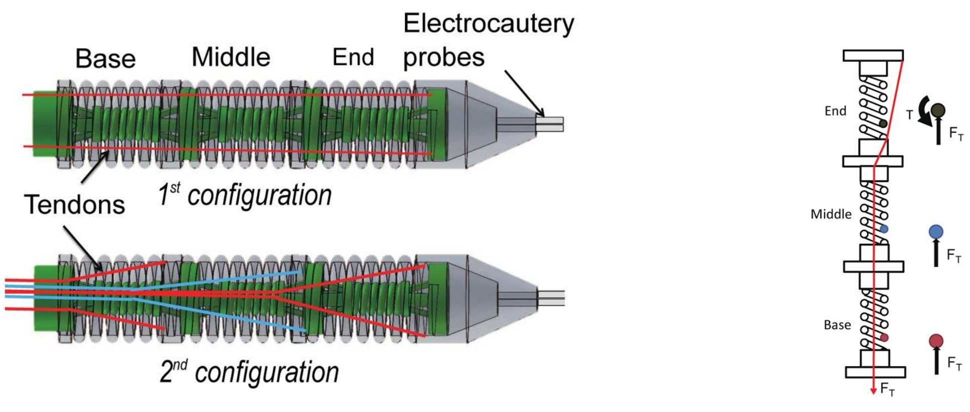

(a) (b)

Figure 2.6: MINIR tendon rearrangement to decouple the continuum segments of the robot (Kim et al., 2017). The 1^{st} configuration (a) depicts the standard routing of tendons which results in the coupling of the segments. The 2^{nd} configuration (b) depicts the tendon arrangement such that the force is normalised and the segments decoupled.

Minimally Invasive Neurosurgical Intracranial Robot (MINIR) is a flexible spring based MRI-compatible tendon driven robot made out of plastic with interconnecting inner and outer springs actuated with SPA using a tendon driven mechanism (Kim et al., 2017). The endoscope is divided into three parts; base, middle and end-segment, with a total length of 60 mm and a diameter of 12.6 mm. A free lumen in the centre of diameter 3 mm is used to house the electrocautery wires and the suction and irrigation tubes (Kim et al., 2017). The snake-like body is actuated in 2 Degrees of Freedom (DOF) with antagonistic pairs of tendons 90° apart. In most tendon-driven endoscopes, the tendons are routed through the periphery of the endoscope, as is depicted in Figure 2.6a, however in MINIR, the tendons are routed through the central axis of the interconnected springs and only branches out at the target segment, shown in Figure 2.6b (Kim et al., 2017). This normalises the force and decouples the continuum segments of the robot.

2.4.2 STIFF-FLOP

Stiffness Controllable Flexible and Learnable Manipulator for Surgical Operation (STIFF-FLOP), is a European project that consists of a modular variable-stiffness flexible endoscope inspired by an octopus arm (Cianchetti et al., 2013). Three iterations of the design were made with versions 1 and 2 having granular jamming for stiffness control and versions 2 and 3 having a free lumen in the centre. These can be seen in Figure 2.7. The first design is manufactured using flexible elastomer making it compliant. It is actuated and bent in several directions with the pressurization of three pneumatic chambers equally spaced in a radial arrangement. A braided sleeve is attached to the distal outer radius of the endoscope to limit any radial expansion. The outer diameter of the complete module is 32 mm (Cianchetti et al., 2013). The granular jamming implemented with the use of a latex membrane filled with coarse coffee powder is inserted into an 8 mm channel which stiffens when vacuum is applied to the chamber.

The second design is based on the improvements made from the first. This included freeing up the central channel to create a free lumen by removing the granular jamming. Instead it is placed equidistant in a radial arrangement along with the actuation chambers such that the two alternate. The actuation chambers are made to have cylindrical cross-section with braided sheath around each chamber instead of an external sheath, which was removed (Cianchetti and Menciassi, 2017).

Generation	I	II	III
External diameter	35 mm	25 mm	14.7 mm
Module length	50 mm	50 mm	55 mm
FFA shape	Half cylinder	Cylinder	Cylinder
Containment method	External with braided sheath	Internal with helicoidal threads	Internal with helicoidal threads
Tubing	Through the silicone body	Inside the inner channel	Inside the inner channel
GJ position	Inside the inner channel	Between FFAN	N/A
Free space in the inner channel	Not usable	Lodging tubes	Lodging tubes
Cross section sketch	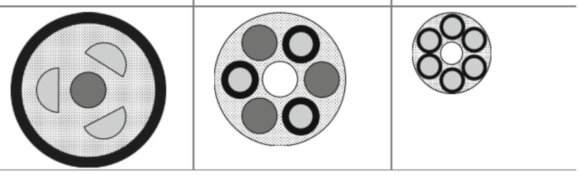		

Figure 2.7: Design and specifications of the each STIFF-FLOP design iteration (Cianchetti and Menciassi, 2017)

The third and final design was made much smaller, with an outer diameter of 14.5 mm. This was achieved by removing the granular jamming entirely and using the free space to implement additional pneumatic actuators (Abidi et al., 2017). To maximise the bending moment and stability, actuators were pressurized in pairs. Both versions 2 and 3 were tested on human cadavers, proving their reaching and bending capabilities.

2.4.3 MOLLUSC

Based on the STIFF-FLOP, Multi-Level Stiffness Controllable (MOLLUSC), depicted in Figure 2.8, works on improving the endoscope functionality by implementing stiffness control with a free-central lumen and actuating with 2 antagonistic pneumatic pairs for a more intuitive control. The chambers are used for both bending and stiffness (Gifari, 2018). Although the MOLLUSC can achieve higher bending angle for multi-chamber bending compared to STIFF-FLOP, the granular jamming implemented reduces the overall bending possibility of the endoscope. The endoscope designed was also much larger than the traditional trocar, with a distal radius of 30 mm.

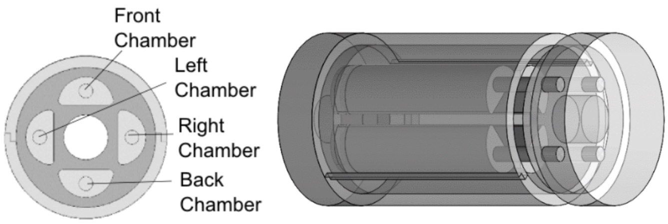

Figure 2.8: Design of the MOLLUSC with antagonistic actuation chambers and a free central lumen with 3D CAD drawing of mould (Gifari, 2018).

2.5 State-of-the-Art Endoscopes

Flexible endoscopes that provide the aforementioned capabilities for MIS are Invendoscope (produced by Invend Medical GmbH, Germany), NeoGuide (produced by NeoGuide Endoscopy System Inc.) and gastroscopes by Olympus. They are not MRI-compatible, however, design ideas can be extracted from them as they are FDA approved and currently used in surgeries.

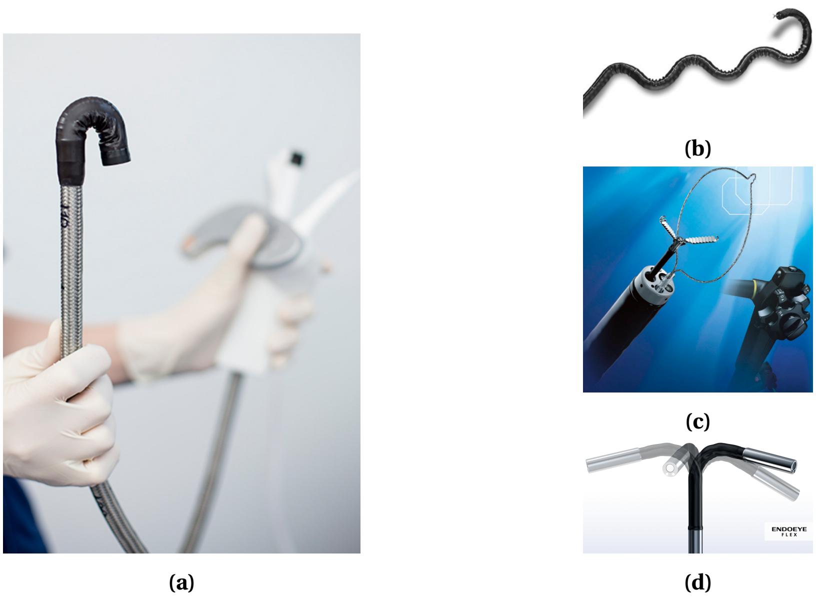

Figure 2.9: State of the art endoscopes and robotic systems currently used to perform surgery. The Endoscopes depicted here are: (a) the Invendoscope (Yeung et al., 2019), (b) the NeoGuide (Yeung et al., 2019), (c) the Dual-Channel Endoscope by Olympus (Olympus, 2020) and (d) the flexible video laparoscope by Olympus (Olympus, 2019).

Invendoscope: Invendoscope (produced by Invend Medical GmbH, Germany) is a single-use colonoscope with a reusable hand-held controller. It is a robotically controlled endoscope with an insertion tube of 170 cm in length, with a distal tip that can bend 180° in all directions (Yeung et al., 2019). An inner free lumen of 3.1 mm enables the insertion of standard flexible instruments (Peters et al., 2018). The endoscope is self-propagated with a driving unit consisting of 8 wheels driving it into and out of the colon (Kahi et al., 2013).

NeoGuide: NeoGuide Endoscope system (developed by NeoGuide Endoscopy System Inc. Los Gatos, CA) is a 16 segment colonoscope that is computer aided such that each segment can be programmed to change shape and follow the lead segment as it travel deeper into the colon (Seah et al., 2017; Peters et al., 2018). The endoscope is 173 mm long with a tapering diameter from 20 mm at the base to 14 mm at the tip. The working channel located at the centre is 3.2 mm in diameter (Kahi et al., 2013).

Olympus: Olympus produces various flexible endoscopes, primarily for gastroscopy and colonoscopy. Their top functioning endoscope is the dual-channel endoscope (DCE) that enables the insertion of two surgical instruments simultaneously however lacks in bi-manual instrument coordination (Yeung and Gourlay, 2012). It has a distal diameter of 12.2 mm with 2.8 mm and 3.7 mm free central channels and a working length of 1030 mm (Olympus, 2020). ENDOEYE FLEX is another flexible endoscope developed my Olympus specifically for laparoscopy with an outer diameter of either 5.4 mm or 10 mm, functioning purely as a videoscope and therefore has no central free lumen (Olympus, 2019).

2.6 Literature Summary

A summary of the flexible endoscopes can be found in Table 2.2 with comparisons based on the outer diameter, number of free lumen and their diameters, maximum bending, MRI-compatibility, variable stiffness and trackability.

STIFF-FLOP version 3 and Olympus ENDOEYE FLEX are the only two endoscopes analysed that are designed specifically for laparoscopy. Based on the outer diameter, it is clear that ENDOEYE FLEX would fit through traditional laparoscopy trocars, however, the same cannot be said for the STIFF-FLOP or any other device analysed here. Those with a free central lumen have lumen diameters ranging from 2.8 mm to 4.5 mm enabling the insertion of surgical instruments and cameras. This functionality is not available for STIFF-FLOP version 1 and ENDOEYE FLEX, where the latter is used purely for visual feedback.

All of the state-of-the-art endoscopes that are FDA approved and currently being used in surgeries are unfortunately not MRI-Compatible. NeoGuide, along with MOLLUSC and STIFF-FLOP versions 1 and 2, have variable stiffness mechanisms activated using semi-active actuators that change their elastic property (Gifari, 2018). The mechanism used for stiffening in all but NeoGuide is granular jamming. Advantages of MRI-compatible endoscopes is that they can be tracked and localized using MRI. All state-of-the-art endoscopes are not MRI-compatible while all flexible soft endoscopes currently being developed are made entirely of MRI-compatible materials. NeoGuide uses depth position sensor as well as path planning for localization (Peters et al., 2018).

Table 2.2: Summary of flexible endoscopes discussed

Technology	Outer Diameter (mm)	Free Lumen # /Diameter(mm)	Max Bending	MRI-Compatible	Variable stiffness	Trackability	Functionality
MINIR	12.6	1/3.0	90 °	Yes	No	Yes	Neuroendoscopy
STIFF-FLOP (V1)	35.0	n/a	120 °	Yes	Yes	Yes	NOTES
STIFF-FLOP (V2)	25.0	1/4.0	120 °	Yes	Yes	Yes	NOTES
STIFF-FLOP (V3)	14.7	1/4.5	120 °	Yes	No	Yes	Laparoscope
MOLLUSC	30.0	1/~	100 °	Yes	Yes	Yes	NOTES
Invendoscope	18.0	1/3.1	180 °	No	No	No	Colonoscopy
NeoGuide	20.0-14.0	1/3.2	~	No	Yes	Yes	Colonoscopy
Olympus ENDOEYE FLEX	10.0/5.0	n/a	100 °	No	No	Yes	Laparoscopy
Olympus DCE	12.2	2/2.8,3.7	140 °	No	No	No	Gastroscopy

3 Design of Soft Pneumatic Endoscope

This chapter details the design process beginning with the design requirements, determined based on the literature review performed in Chapter 2, and ending with the final design. The intermediate steps are depicted in Figure 3.1.

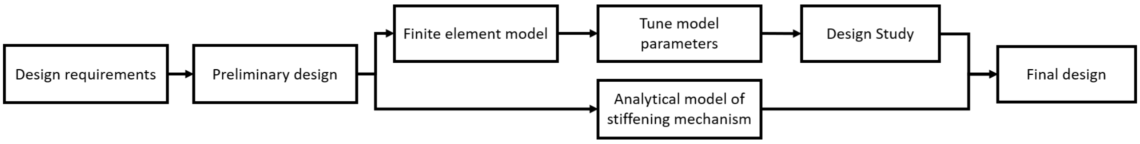

Figure 3.1: Overview of the design process

A preliminary design based on the design requirements, consists of two main components, the pneumatic actuation mechanism and the stiffening mechanism. Both aspects of the design are analysed to determine the parameters that influence the performance the endoscope. The pneumatic actuation is modelled and assessed using FEM and the model parameters are tuned to match the real world performance. A design study is then performed focusing on three key design parameters to determine their influence on the performance of the endoscope. Additionally, an analytical model of the stiffening mechanism is made. The final design is determined based on the results of the FE and the analytical model analysis.

3.1 Requirements

The design requirements for a soft endoscope capable of performing laparoscopy are based on the literature review performed in Chapter 2 and the research goals set in Chapter 1. They are:

1. The size of the endoscope is dependent on the application, therefore, development of a MIS endoscope capable of also performing laparoscopy must have an outer diameter less than or equal to 12 mm, such that it can fit into traditional trocars.
2. A modular design allows for a customisable endoscope based on the requirement of the surgery. Therefore, the design must be modular where each module can be individually controlled.
3. The design must also be scalable such that the modules can be stacked.
4. A free central lumen for the insertion of medical tools, camera and other cables is required. Based on the literature review, the central lumen must be between 2.8 mm to 4.5 mm in diameter.
5. The variable stiffness mechanism must be designed such that the endoscope tip can apply forces between 0.9 N to 3.3 N (Blanc et al., 2017).
6. The endoscope must be designed such that the bending performance is linear at near-straight configuration. Therefore, the dead zone must be shifted or removed entirely. Near-straight configuration is defined as between 0° and 20°.
7. The endoscope must be MR-compatible for localisation and increased functionality.

3.2 Preliminary Design

The main driving factors in formulating a preliminary design is shifting the dead zone. As mentioned in Section 1.3, the dead zone is a product of the fabrication process of pneumatic actuators and is primarily a result of the free-space between the actuation chamber and the external sheathing. To shift the start-up transient in the bending performance, such that it is not in the operating range, the endoscope starts pre-bent. Therefore, unlike the endoscope designed by Lin (2019) and the STIFF-FLOP, the novel endoscope designed begins bent when at rest and straightens when actuated.

The preliminary design is based on the single chamber shell-reinforced SPA, explained in Section 2.2, which is modified to meet the rest of the requirements outlined in Section 3.1. Matching the performance of the endoscopes presented in Chapter 2, the maximum bending angle of the module is set to 120°. Therefore, when not actuated, the endoscope tip is at an angle of 120°.

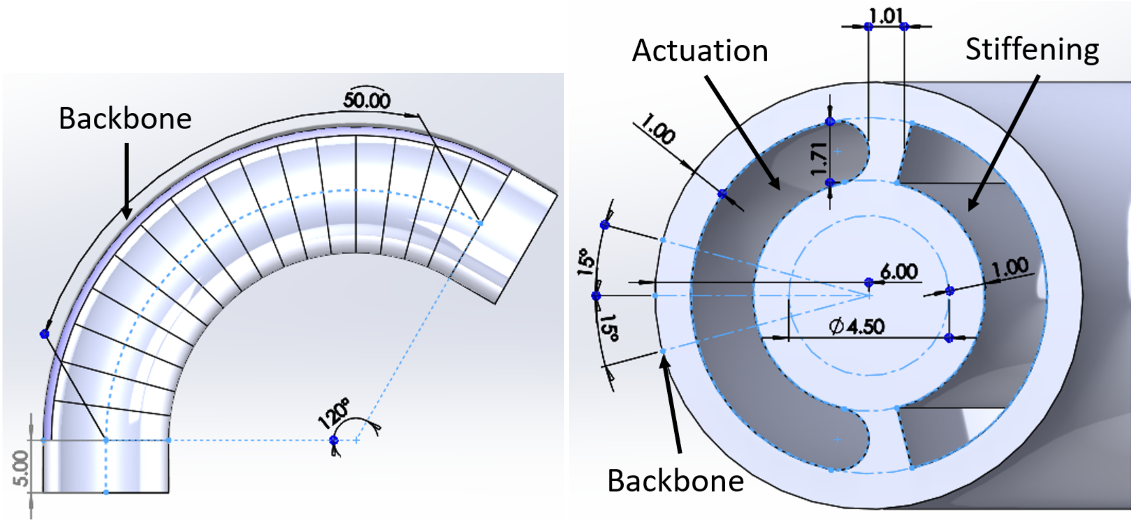

(a)

(b)

Figure 3.2: Preliminary design of the endoscope module. (a) is the outline of the preliminary design with a central arc of 50 mm and an initial bending angle of 120°. (b) shows the orientation and sizes of the actuation and stiffening chambers. The backbone is placed along the outer arc and therefore next to the actuation chamber. The gap between the chambers and outer diameter of the module is 1 mm.

The shell-reinforcement designed is similar to that used in the bending SPA, with rings attached to a backbone that runs along the outer arc of the bent actuator instead of the inner arc, as is shown in Figure 2.2. Thus, the rings are further apart along the outer arc and closer together along the inner arc. When the actuator is pressurised, the backbone will inhibit the extension of the module and will instead bend in the direction of the force applied along the former. The shell-reinforcement consists of 16 rings and a backbone of width 3 mm. A high number of rings were chosen to reduce ballooning and the backbone width is chosen arbitrarily.

As has been explained, the endoscope designed will be modular, therefore each module must be individually controlled. The length of the modules is set to 60 mm, with a 50 mm curved central arc and a 5 mm cap on both ends. Once again, the modules length is chosen to match the performance and capabilities of endoscopes presented in Chapter 2. The outer diameter of the endoscope is set to be 12 mm so that it can fit in traditional trocars.

Another requirement for a MIS endoscope is to have a free central channel required for the implementation of a camera, or to insert medical tools. The size of the central channel is dependent on the application of the endoscope. If it is required for exploration purposes only, then it must be fitted with a camera, however, if a biopsy needs to be performed, the endoscope is equipped with a camera and surgical tools. As the endoscope is pneumatically actuated and is a modular design, it must also house the pneumatic tubes of stacked modules. Thus, matching the clinically tested endoscopes, the size of the central lumen is set to be 4.5 mm.

The variable stiffening mechanism chosen is laminar jamming, based on the results of the literature review found in Table 2.1. The orientation of the actuation chamber and the stiffening mechanism can be seen in Figure 3.2. Here the actuation chamber is located along the backbone, thus along the outer arc, while the stiffening mechanism is opposite to it, thus along the inner arc. This is because when pressure is applied directly to the backbone it will induce a motion to bend in the direction of the applied force and would consequently straighten up. The area of the chambers chosen is such that the actuation chamber spans along half of the circumference of the endoscope while the stiffening chamber is along the other half.

Since there are portions of the endoscope that are not entirely covered by the shell-reinforcement, an additional sheathing is required to constrain any radial expansion. This will strengthen the module by adding stiffness as well as drastically decreasing the chances of mechanical failure at high pressures due to ballooning and rupture.

Table 3.1: Summary of preliminary design parameters.

Requirements	**Value**
Outer diameter	12 mm
Module Length	60 mm
Central lumen diameter	4.5 mm
Max bending angle	120°
Force requirement	0.9 N - 3.3 N
Cross-sectional area - Actuation Chamber	$\frac{1}{2}$ of circumference
Number of rings	16
Backbone Width	3 mm

Bending Angle:

The definition of the bending angle used throughout this report is explained here. The bending angle is defined as the rotation of the coordinate frame at the endoscope tip with respect to the fixed coordinate frame at the origin. Assuming piecewise constant curvature of the endoscope and pure rotation about the z-axis, the angle of rotation of the coordinate frames is expressed by $180-2\theta$, where θ is the angle between the x-axis and the vector between the origin (O) and the endoscope tip (EE). Positive rotation of the coordinate frame on the endoscope tip is defined in the anti-clockwise direction. At rest, the endoscope begins with a bending angle of $-120°$ with respect to the fixed coordinate frame O.

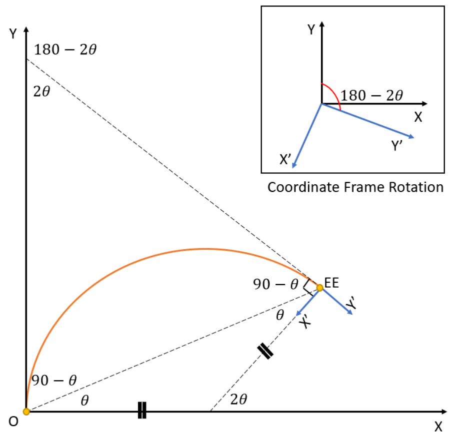

Figure 3.3: The method of calculation of the bending angle. O is the origin and EE is the end-effector.

The preliminary design contains two mechanisms: the actuation and stiffening mechanisms. Both of these aspects are modelled and their performance is analysed using FE and analytical modelling, respectively, such that the performance of the final endoscope is improved. This is explained in further detail in the following sections.

3.2.1 Finite Element Model

The FE model is of a simplified version of the preliminary design consisting of only the actuation chamber with a ‘filled’ central lumen and stiffening mechanism. When in use, the central lumen of the endoscope will be filled with a camera and other surgical tools. Therefore, in simulation it has been modelled as filled. The simplified design can be seen in Figure 3.4. Only half of the endoscope is modelled to reduce computation time and therefore symmetry is defined along the plane of cut.

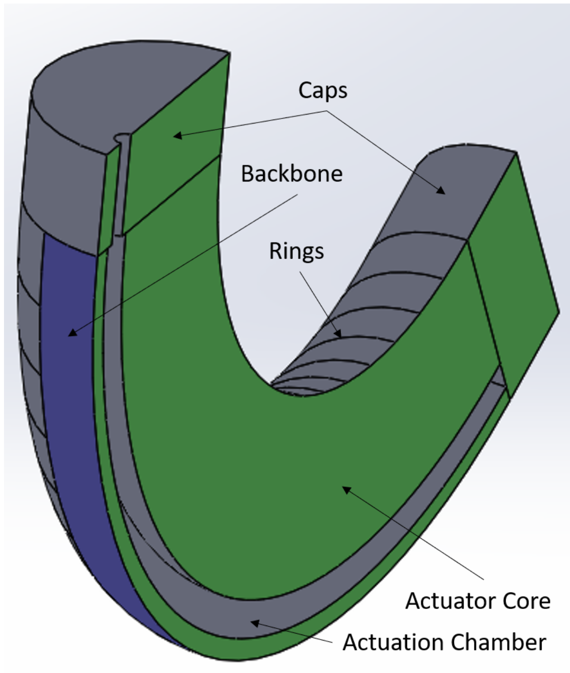

Figure 3.4: Simplified preliminary design of the endoscope module used for FE simulations. The backbone has been highlighted with the blue strip running along the outer arc of the endoscope. The rings, depicted as curved edges, are attached to the backbone and run along the circumference of the module. The plane of symmetry has been highlighted by the green faces.

COMSOL Physics

The FE model can be divided into three parts: the body, the backbone and the rings. Each part has been modelled as a different structural mechanics interface. The body consists of the actuator core and the caps at both ends. They are modelled as solids and therefore have the solid mechanics interface. The backbone, which is part of the shell-reinforcement, is a thin flat structure that is inextensible but has no bending stiffness. This is, therefore, modelled as a membrane. Finally, truss elements are assigned to the rings which are attached to the backbone at their inter-sectional nodes and are also made of inextensible material. All three have a quasi-static transient behaviour and quadratic discretisation.

The boundary load is applied on all inner walls of the actuation chamber with pressure incrementing from 25 Pa to 60000 Pa. The membrane has a thickness of 0.2 mm while the truss has a rectangular cross-sectional area of 0.2 mm.

Material Properties

The body, as mentioned above, consists of the actuator core and the caps. The caps are modelled as linear elastic isotropic with the material properties of acrylic, chosen because of its high stiffness. When actuated the caps should not be influenced by the pressurisation of the chamber. Although the caps are modelled as acrylic, they will not be fabricated as such. This is only for the purpose of modelling the caps to be very stiff. The actuator core, with the filled central lumen and stiffening chamber, is modelled as the hyper-elastic material: Ecoflex 00-30. The later was chosen because uni-axial hysteresis only becomes prominent for strains higher than 0.75 (Ahmad et al., 2019), unlike, Ecoflex 00-50 where it became prominent for strains higher than 0.2.

The hyper-elastic material model chosen is Neo-Hookean, which has shown to be a suitable material model for Ecoflex as it exhibits less problems with element distortion in large deformations. The model captures the non-linear behaviour of the material while having good physical interpretation of the parameters (Irving et al., 2004; Boonvisut et al., 2012). The strain energy density function W of the Neo-Hookean material model is

$$W = \frac{1}{2}\left(\mu(i_1 - 3) - \mu \log(i_3) + \lambda(\sqrt{i_3} - 1)^2\right) \tag{3.1}$$

Here, λ and μ are Lamé‘s first and second parameters respectively and, i_1 and i_3 are the invariants of the Cauchy-Green deformation tensor C. Lamé's parameters are a function of Young's Modulus E and the Poisson ratio v with the following relation:

$$\lambda = \frac{Ev}{(1+v)(1-2v)} \tag{3.2}$$

$$\mu = \frac{E}{2(1+v)} \tag{3.3}$$

and the invariants of the Cauchy-Green deformation are defined by i_1 = trace(C) and i_3 = det(C) (Boonvisut et al., 2012). The shell-reinforcement is modelled as paper coated in plastic, a built-in material in COMSOL. This was chosen because paper has almost no bending stiffness but is also inextensible. All parameter values can also be found in Table 3.2.

Table 3.2: The elastic modulus, Poisson ratio and density implemented into the FE model.

Material	**Young's Modulus (E)**	**Poisson's Ratio (v)**	**Density (kg/m^3)**
Ecoflex 00-30	27.04 kPa	0.43	1000
Acrylic	3.2 GPa	0.35	1190
Paper-coated-plastic	200 GPa	0.20	940

Mesh

The caps, compared to the rest of the components, have been meshed differently. Since the caps are modelled as rigid and linear elastic with high stiffness, they are expected to undergo no or very limited deformation and therefore were meshed with a coarse meshing setting. The coarse meshing has a maximum and minimum element size of 7.48 mm and 1.4 mm respectively. The body and the shell-reinforcement are the regions of interest and the areas with highly non-linear behaviour. Therefore, the mesh size is set to extra fine. The extra fine mesh has a maximum and minimum element size of 1.75 mm and 0.0748 mm respectively. The element type chosen is the default free tetrahedral.

The measure used to determine the mesh quality is skewness. The skewness measure is based on the equiangular skew and penalises elements with large and small angles when compared to the angles in an ideal element. The minimum element quality of the mesh for the entire geometry is 0.24 while the maximum element quality of the mesh is above 0.67. The element quality ranges from 0 to 1 with 1 being the best possible quality with the optimal element chosen.

3.2.2 Model Validation

The FE model is created using the aforementioned specifications. By fabricating the FE model and comparing its bending performance to the simulation results, the FE model can be tuned until the two bending performances match, thereby validating the latter. In Figure 3.5 it can be seen that the simulation results of the FE model, depicted in dark blue, behave differently when compared to the real world experimental results of the bending performance, depicted in maroon.

The fabricated FE model, which consits of only an actuation mechanism, has a start-up behaviour, very much like the one seen in Figure 1.3. This is followed by a linear regime which seamlessly merges into non-linear behaviour towards the end. Comparatively, the simulated result does not show this behaviour and is linear throughout. Therefore, to compare the experimental and simulation results, a linear curve is fitted through the former using Matlab's curve fitting toolbox. The simulation results are then compared to the linear fit. The parameters of the first order polynomial are $p_1 = 243.5$ and $p_2 = -102$ with their 95% confidence bounds $(242.8, 244.2)$ and $(-102.1, -101.8)$ respectively. The root-mean-square estimate of the fit is 0.59 while the R-square is 0.99. The R-square is a square of the correlation between the response value and the predicted response value. Values closer to 1 indicate that a greater portion of variance is accounted for in the model.

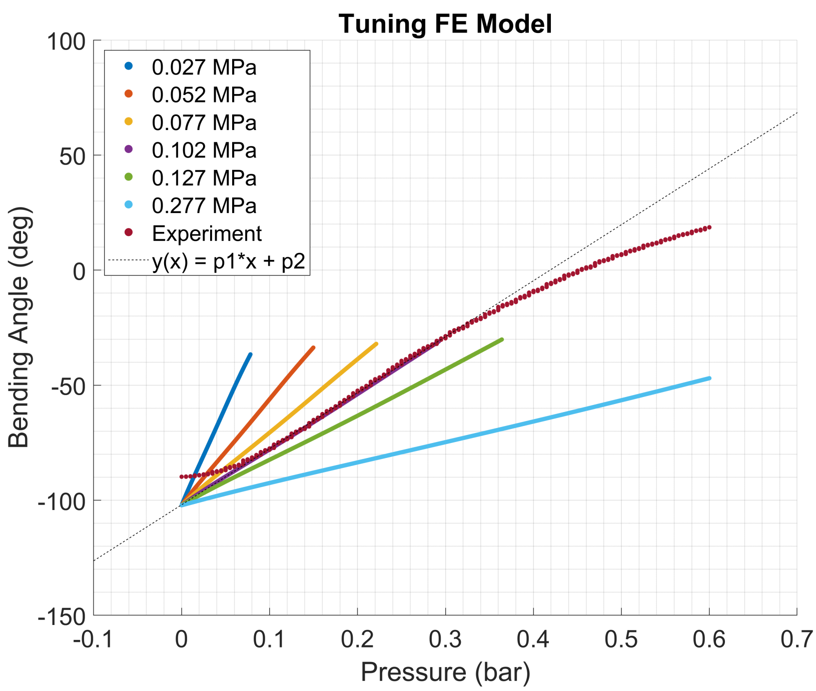

Figure 3.5: Simulation and experimental results of the preliminary design

The FE model does not account for the additional sheathing that encases the main elastomer body of the endoscope when fabricated. Therefore, the material properties defined do not match the fabricated endoscope. Thus, the FE model is tuned by varying its elastic modulus, E. In Figure 3.5, the Young's Modulus of the hyper elastic material is increased by 25, 50, 75, 100 and 225 kPa. These are depicted by the red, orange, purple, green and light blue lines respectively. As can be seen, a Young's modulus of 0.102 MPa, which is an increase of 75 kPa, results in the simulation matching the linear fit, thus matching the linear motion of the fabricated endoscope. Thus, using the tuned FE model, a design study can be performed by varying geometric parameters outlined below.

3.2.3 Design Study

With the tuned Finite Element (FE) model, various geometries of the design can be varied to determine which affect the performance of the endoscope and which combination has the best performance. The performance is measured using two criteria: *amount of bending for applied pressure and linearity at operating range.* The ideal performance is for the endoscope to bend with as little applied pressure as possible and to also be linear at 0°. The geometries varied will be the cross-section of the actuation chamber, the number of rings attached to the backbone and the width of the backbone. These are depicted in Figure 3.6. The cross-sectional area of the actuation chamber simulated are $\frac{1}{4}$, $\frac{1}{2}$ and $\frac{3}{4}$ of the circumference of the endoscope. The number of rings are varied from 4 to 20 with increments of 4 and have a rectangular cross-section of 0.2 mm. The width of the backbone is determined by the angle between the centre line of the endoscope when viewed from above and the outer-edge of the backbone. The backbone width is therefore varied between 15° to 60° with increments of 15°. The thickness of the backbone is set to 0.2 mm. All simulations have input pressure from 25 Pa to 60000 Pa with increments of 25 Pa.

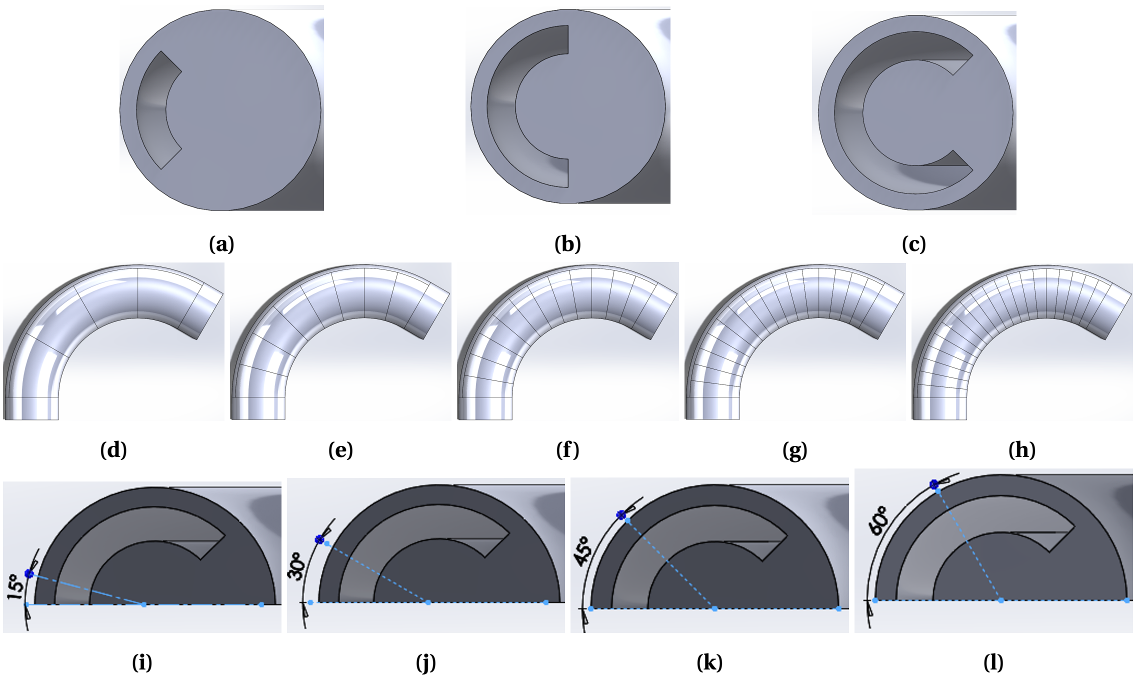

Figure 3.6: The geometric variations for the design study. (a - c) depicts the cross-sectional area of the actuation chamber, (d - h) depicts the number of rings and (i - l) depicts the backbone width.

The first study conducted is varying the cross-sectional area. All other parameters of the models are kept constant and consistent with those of the preliminary design. Therefore, the number of rings and backbone width are 16 and 15°, respectively. Based on the results of the first study, the design will be improved. For the next study, where the number of rings are varied, the cross-sectional area of the models is that which performed best while the width of the backbone is kept at 15°. Through this iterative process, the final study, with varying backbone width, should consist of a model that has the best performance. All other geometric and material properties of the designs that are not being varied or tested are kept constant and can be found in Table 3.1 and Table 3.2.

Cross-Sectional Area

The cross-sectional area is proportional to the bending moment and therefore directly influences the bending performance. A larger cross-sectional area should result in a larger bending moment and thus a larger bending angle for an applied pressure. In Figure 3.7 the simulation results of the bending performance of models with varying cross-sectional areas are shown. Along the x-axis is the increasing pressure and along the y-axis is the bending angle. Here, a larger cross-sectional area performs better, that is, the endoscope bends more for a lower applied pressure. The performance however is not linear at near-straight configuration. In fact, the simulation does not reach a bending angle of 0°. This will be discussed in further detail in the discussion below. Therefore, in terms of the amount of bending for applied pressure, the best performance is of the largest actuation chamber with a cross-section of $\frac{3}{4}$. The drawback of having a large actuation chamber is that it does not leave a lot of space for the implementation of the stiffening mechanism.

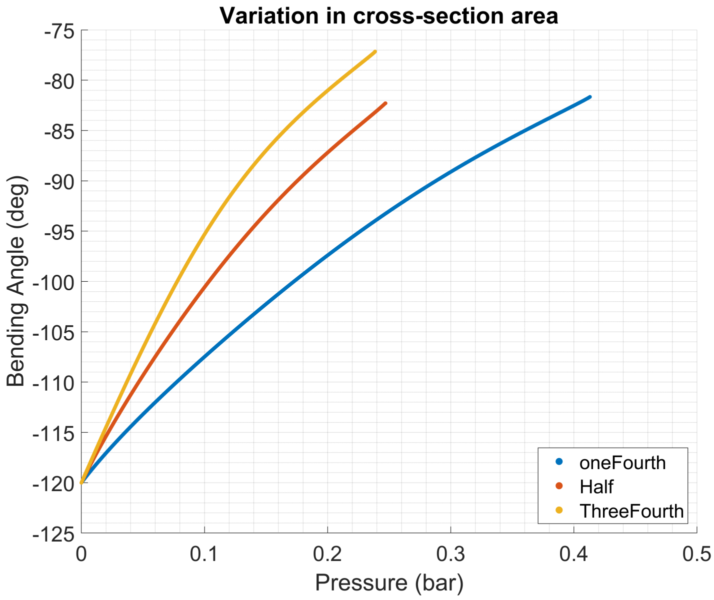

Figure 3.7: Simulated bending performance of models with varying cross-sectional areas of the actuation chamber.

Number of Rings

Agarwal et al. (2016) show that the ballooning during actuation decreases with a larger number of rings encasing the shell-reinforced SPA. Therefore, it is expected that the bending performance of the endoscope improves with larger number of rings as it will experience less strain. In Figure 3.8 the simulation results of models with varying number of rings is shown. In Figure 3.8a, it can be seen that the behaviour at the beginning is similar for all models, however, they start to deviate at different input pressures. For example, the model with 4 rings, depicted in blue, deviates from the initial motion at an input pressure of 0.06 bar after which it begins to bend more for a given input pressure, indicating improved bending performance. However, its maximum bending is affected, reaching an angle of 88° before eventually stopping due to convergence errors. The improved performance indicates that the stiffness of the model decreases compared to the rest and is a result of ballooning. Ballooning weakens the actuator wall by decreasing its thickness which in turn decreases its stiffness.

This phenomenon can be seen clearly in Figure 3.8b. It depicts the Von Mises stress plotted with respect to the bending angle. The stress plotted is at the contact point between rings and the backbone. It shows that the stress experienced is much larger for the model with 4 rings compared to the model with 20 rings for a given bending angle. This indicates that as the elastomer balloons, there are larger forces experienced at the contact point, thus indicating larger strains in the elastomer. Therefore, although the model with the largest number of rings is stiffer, it experiences lower stress thereby decreasing the negative effects of ballooning and potential rupture.

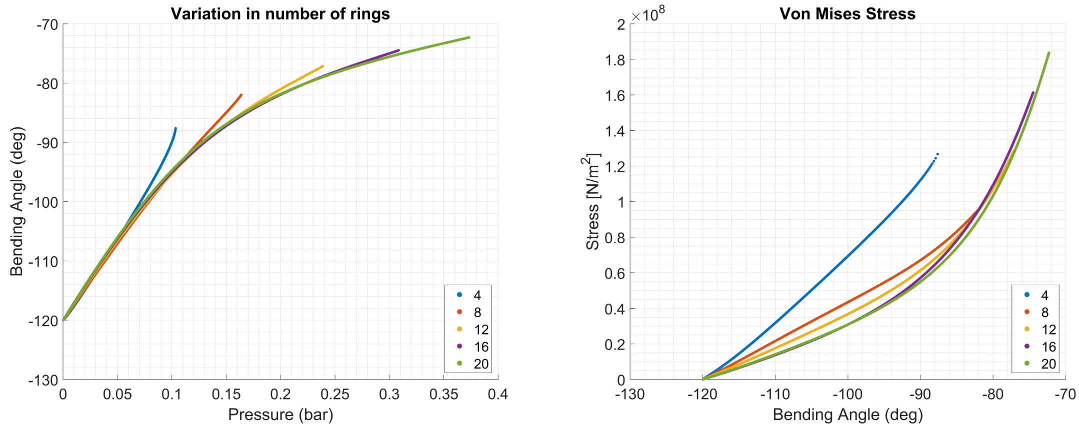

(a) (b)

Figure 3.8: Simulated performance of models with varying number of rings attached to the backbone. (a) depicts the bending performance, that is bending angle with respect to applied pressure and (b) depicts the Von Mises stress experienced with respect to the bending of the endoscope tip.

Backbone Width

The backbone is a significant part of the design, running along the outer arc of the endoscope. The thickness of the backbone is restricted as it is dependent on the maximum outer diameter of the endoscope. The width, however, can be varied. Since the backbone is modelled as an inextensible material, a larger backbone width should increase the stiffness of the model and therefore inhibit the bending performance. In Figure 3.9 the simulation results of models with varying backbone width are shown. In Figure 3.8a, it can be seen that a larger backbone width increases the stiffness of the model and therefore has poorer bending performance. The backbone width of 15° performs best since it bends more compared to the rest for a given applied pressure. The latter also has linear motion till approximately 0.04 bar.

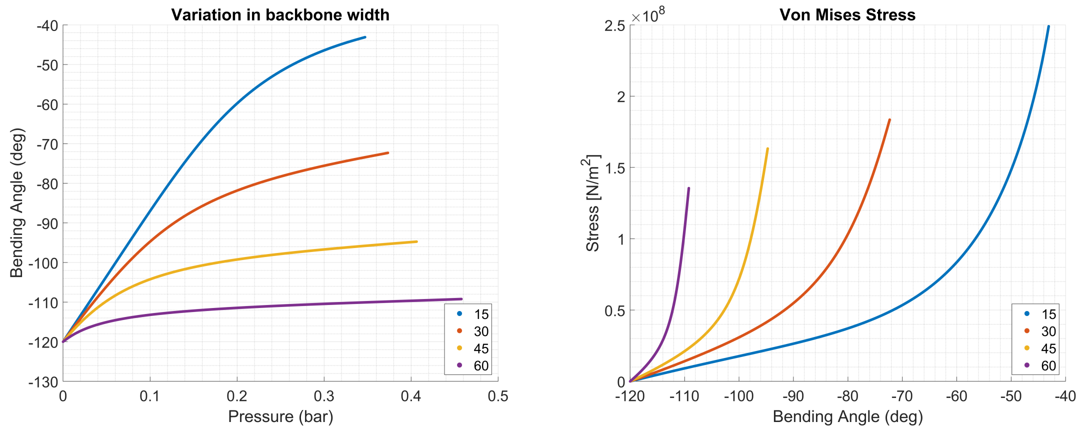

(a) (b)

Figure 3.9: Simulated performance of models with varying backbone width. (a) depicts the bending performance, that is bending angle with respect to applied pressure and (b) depicts the Von Mises stress experienced with respect to the bending of the endoscope tip.

Figure 3.9b corroborates that a smaller backbone width decrease the stiffness of the model. The stress experienced by the model with a backbone width of 15° is significantly lower than for the models with a larger backbone width. Therefore, the model with the lowest backbone width performs best.

Discussion and Conclusion

Geometric properties such as the cross-sectional area, the number of rings and the width of the backbone all effect the performance of the endoscope. As mentioned above, the performance is analysed based on two criteria: the amount of bending with respect to applied pressure and linearity at operating region. Since none of the simulations reached the operating region due to convergence errors, the models are assessed based on their bending performance. Convergence errors occur for several reasons. One possible source of error could be due to the excessive deformation of some elements in a short time such that the convergence criteria could not be satisfied. A solution for this would be refining the mesh size, however this will lead to an increase in computational time.

Another source of error could be that the stiffness matrix is ill-conditioned due to the very high aspect ratio of the geometry. The aspect ratio occurs by modelling thin elements, like a shell, with solid elements within the COMSOL structural mechanics physics module. This can be determined by forcing the solver to return a solution unless the stiffness matrix is singular.

In conclusion, based on the design study performed, the models that performed best are those with a larger cross-sectional area, larger number of rings and smallest backbone width.

3.2.4 Analytical Model of Stiffening Mechanism

Laminar jamming consists of layers of sheets which when clamped together become very stiff due to the increased static friction between layers, interlocking them together. Two states of the stiffening mechanism will be analysed: the compliant state, when the mechanism is not activated and the stiff state, when the stiffening mechanism is activated. In the compliant state the layers are separated from each other and therefore behave has individual beams. In the stiff state, the layers are merged and therefore behave as a singular beam. These states are depicted in Figure 3.10b and Figure 3.10c, respectively. This analytical model will be used to determine the lower and upper bounds of the bending stiffness of the variable stiffening mechanism.

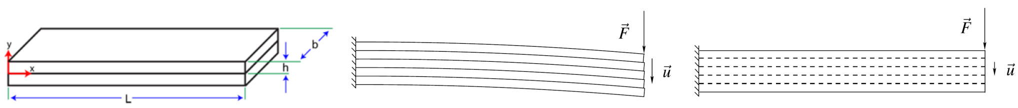

(a) **(b)** **(c)**

Figure 3.10: Diagram used for analytical derivation of governing equations derived from the research of Narang et al. (2018). (a) depicts the coordinate system and the dimensions of the simplified two layer stiffening mechanism. (b) depicts the compliant state of the stiffening mechanism with each layer behaving like a separate beam and (c) depicts the stiff state of the stiffening mechanism behaving like a cohesive single beam (Henke and Gerlach, 2014).

The model is based on the research performed by Narang et al. where a two layered jamming structure is modelled. Here, the layers are stacked on top of each other and fixed on one end, behaving like cantilevered beams. The origin is located on the left edge of the structure at the interface of the two plates. The length, height and breath are as is depicted in Figure 3.10a. The structure will be loaded in the transverse direction with a uniform distributed load ω.

Using Euler-Bernoulli beam theory, the axial strain fields in the layers of the jamming structure are:

$$\epsilon_1(x,y) = -\kappa(x)y \tag{3.4}$$

$$\epsilon_2(x,y) = -\kappa(x)y \tag{3.5}$$

where, $\epsilon_1(x,y)$ and $\epsilon_2(x,y)$ are the axial strains in the bottom and top layers respectively and $\kappa(x)$ is the curvature along the interface. The axial stress field for elastic and isotropic layers are:

$$\sigma_1(x,y) = -E\kappa(x)y \tag{3.6}$$

$$\sigma_2(x,y) = -E\kappa(x)y \tag{3.7}$$

Here, E is the elastic modulus of the sheets. The first governing equation is derived by looking at the resultant moment and the axial stress in the jamming structure. The moment-stress relation of a single beam is $M(x) = \int_S -\sigma(x,y)ydS$, where σ is the axial stress and S is the cross-section of the beam. Therefore,

$$M(x) = \int_{S_1} -\sigma_1(x,y)ydS_1 + \int_{S_2} -\sigma_2(x,y)ydS_2 \tag{3.8}$$

$$M(x) = 2\frac{E\kappa(x)bh^3}{3} \tag{3.9}$$

This is the governing equation for a two layered stiffening mechanism. Building on the research performed by Narang et al., the governing equation for a multi-layered stiffening mechanism is:

$$M(x) = \frac{E\kappa(x)bN^3h^3}{12} = EI\kappa(x) \tag{3.10}$$

where, I is the moment area of inertia and is dependent on the breath, height and number of layers within the stiffening mechanism. In this case, the governing equation is for the situation where the stiffening mechanism is activated because the moment area of inertia of the stiffening mechanism is of a cohesive singular beam rather than a collection of beams, depicted in Figure 3.11.

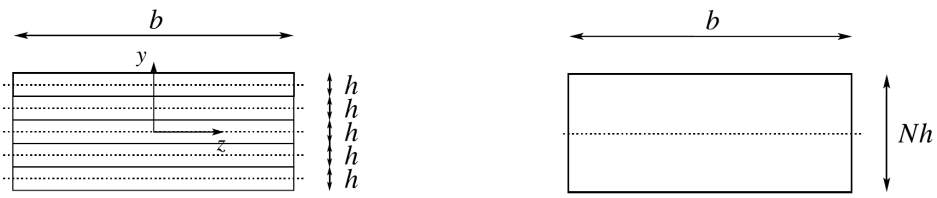

(a) **(b)**

Figure 3.11: The difference in cross-section of a (a) compliant and (b) stiff stiffening mechanism.

The resultant shear force and moment of a cantilever beam clamped at $x = 0$ and loaded with a uniform distributed load are

$$V(x) = -\omega(L-x) \tag{3.11}$$

$$M(x) = \omega Lx - \frac{\omega L^2}{2} - \frac{\omega}{2}x^2 \tag{3.12}$$

equating the governing equation with the moment and solving for $\frac{d^2\omega}{dx^2}$,

$$\frac{d^2W(x)}{dx^2} = -\frac{\omega L^2}{2EI} + \frac{\omega L}{EI}x - \frac{\omega}{2EI}x^2 \tag{3.13}$$

where $\kappa(x) \approx \frac{d^2W(x)}{dx^2}$. Integrating $\frac{d^2\omega}{dx^2}$ to solve for $W(x)$ gives

$$W(x) = -\frac{\omega L^2}{4EI}x^2 + \frac{\omega L}{6EI}x^3 - \frac{\omega}{24EI}x^4 + C_1x + C_2 \tag{3.14}$$

Here C_1 and C_2 are the integration constants. Since the cantilevered beam is clamped, the boundary condition at $x = 0$ results in

$$W(x) = -\frac{\omega L^2}{4EI}x^2 + \frac{\omega L}{6EI}x^3 - \frac{\omega}{24EI}x^4 \tag{3.15}$$

Here the moment area of inertia I is varied depending on whether the stiffening mechanism is compliant or stiff. In the compliant case, $I = N\frac{b(h)^3}{12}$ while in the stiff case the $I = \frac{b(Nh)^3}{12}$. Therefore the stiffness k of the stiffening mechanism is

$$\begin{aligned} k_{min} &= \frac{\omega}{W(x)} = -\frac{8EbNh^3}{12L^4} \\ k_{max} &= -\frac{8EbN^3h^3}{12L^4} \end{aligned} \tag{3.16}$$

The maximum stiffness of the layers is therefore N^2 times larger. Figure 3.12 shows the variation in bending stiffness when the number of layers in the stiffening mechanism are altered. Here, the material and geometric parameters of the sheets are dependent on the preliminary design and their values can be found in Table 3.3.

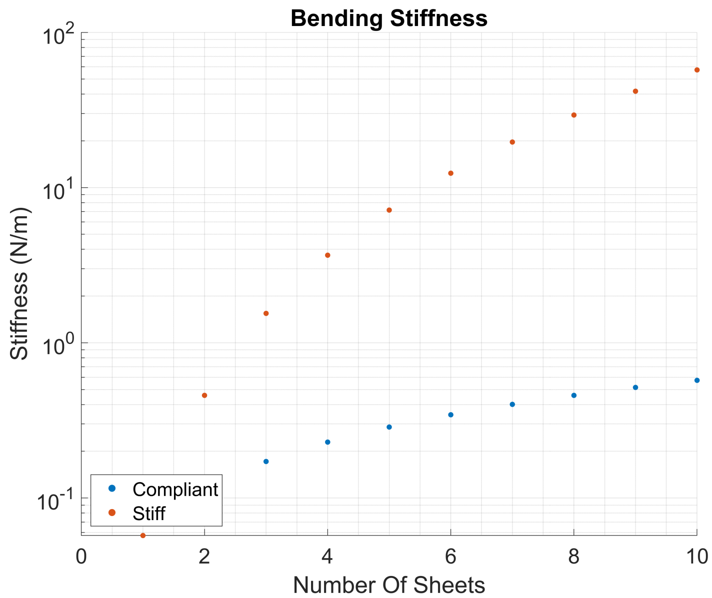

Figure 3.12: The stiffness of the stiffening mechanism for varying number of sheets.

As mentioned above, the variation in stiffness in the compliant and stiff state is dependent on the number of layers and it increases with increasing number of layers. The difference in stiffness between the two states also increases by N^2, as is expected. Given the volume of the stiffening chamber in the preliminary design, 5 laminar sheets can be implements. The upper and lower limit of the stiffness of the jamming structure is then 7.16 N/m and 0.29 N/m, respectively.

Table 3.3: The material and geometric properties of the laminar sheets.

Properties	**Values**
Elastic Modulus (E)	1 GPa
Breath (b)	5.5 mm
Height (h)	0.1 mm
Length (L)	40 mm

3.3 Final Design

The preliminary design is updated based on the FEA of the actuation mechanism and the analytical model of the stiffening mechanism. The results show the cross-sectional area of the actuation chamber can be increased from $\frac{1}{2}$ of the circumference of the endoscope to $\frac{3}{4}$ of the circumference, the number of rings can be increased from 16 to 20 and finally the width of the backbone can remain 15°. However, with a cross-sectional area of $\frac{3}{4}$ of the circumference, there is extremely limited space left for the stiffening mechanism. The stiffness of the laminar jamming mechanism is proportional to the breath of the layers which will be severally limited with the larger actuation chamber. Therefore, the cross-sectional area of the actuation chamber is kept at $\frac{1}{2}$ of the circumference of the endoscope. There are fabrication limitations when going from 16 rings to 20 rings. Thus, the number of rings is also kept the same.

As explained in Section 3.2.4, the stiffness of the stiffening mechanism is dependent on the geometry of the layers themselves as well as the number of layers. For the stiffening mechanism, given the space provided and fabrication limitations, 5 layers are chosen. The parameters of the final design are outlined in Table 3.4.

Table 3.4: Summary of final design parameters.

Requirements	**Value**
Outer diameter	12 mm
Module Length	60 mm
Central lumen diameter	4.5 mm
Max bending angle	120°
Stiffness	7.16 N/m - 0.28 N/m
Cross-sectional area - Actuation Chamber	$\frac{1}{2}$ of circumference
Number of rings	16
Backbone Width	3 mm (15°)
Laminar layers	5

The final design meets all geometric requirements. It is 12 mm in diameter and is a modular design with a single actuation chamber which improves scalability. It has a variable stiffening mechanism implemented, consists of a central free channel and is MR-compatible. The fabrication process of the endoscope is explained in the next chapter.

4 Fabrication

This chapter describes the fabrication process, which is depicted in Figure 4.1. The process is split into three parts: the first is the moulding process which consists of the curing of Ecoflex^{TM} 00-30 by Smooth-On to produce the actuator core and caps. The second involves the fabrication of the shell-reinforcement and its subsequent attachment to the actuator core as well as the fabrication of the stiffening mechanism. The third and final step involves the addition of the braided sheath added to limit the radial expansion of the module entirely.

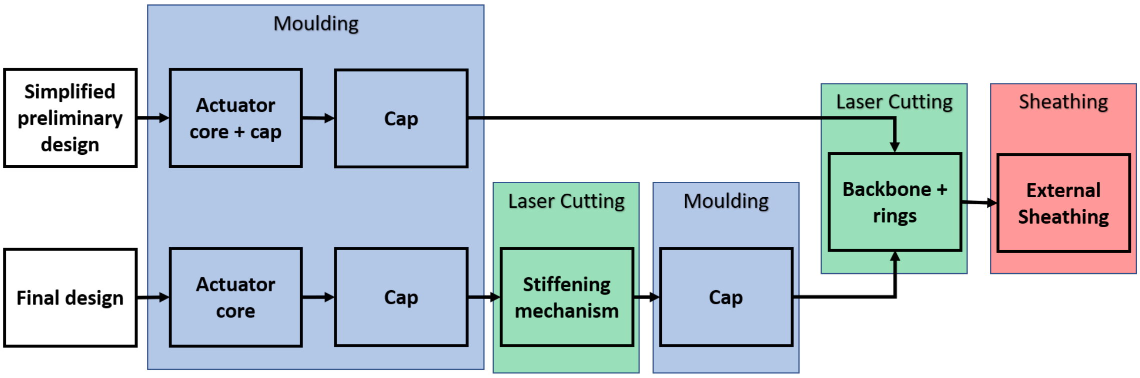

Figure 4.1: The fabrication process for the simplified preliminary design and the final design.

4.1 Moulding

The moulding process is further divided into two sub-parts, the fabrication of the simplified preliminary design and the final design.

4.1.1 Simplified Preliminary Design

The simplified preliminary design is fabricated for the FE model validation, outlined in Section 3.2.2, and consists of only the actuation mechanism. The mould comprises of three parts: the two outer moulds, shown in Figure 4.2a, and the mould of the actuation chamber cavity, shown in Figure 4.2b. One end of the actuation chamber cavity has an extrusion which is used to hold it in place when inserted into the outer moulds. The liquid silicone solution is poured into the outer mould from the top and two air holes at the end let out any trapped air.

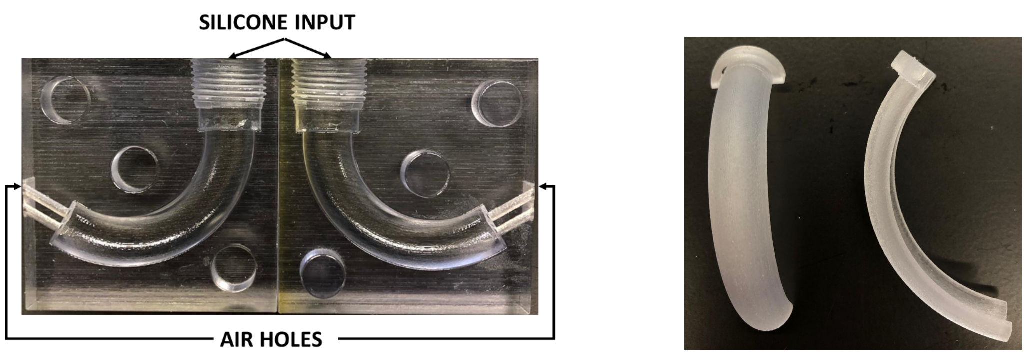

(a) (b)

Figure 4.2: Mould for the fabrication of the simplified preliminary design consisting of only the actuation chamber. (a) the outer moulds and (b) the mould for the actuation chamber cavity.

4.1.2 Final Design

The final design consists of the actuation and stiffening chamber with the central lumen filled in. The moulding process of the final design is similar to that of the preliminary design with an additional mould for the stiffening chamber cavity. In this moulding process, both ends of the cavity moulds are fixed in place with the help of the outer moulds and an additional cap. Once again, the liquid silicone is poured through the open entry point and air holes at the end let out trapped air. The moulds can be seen in Figure 4.3.

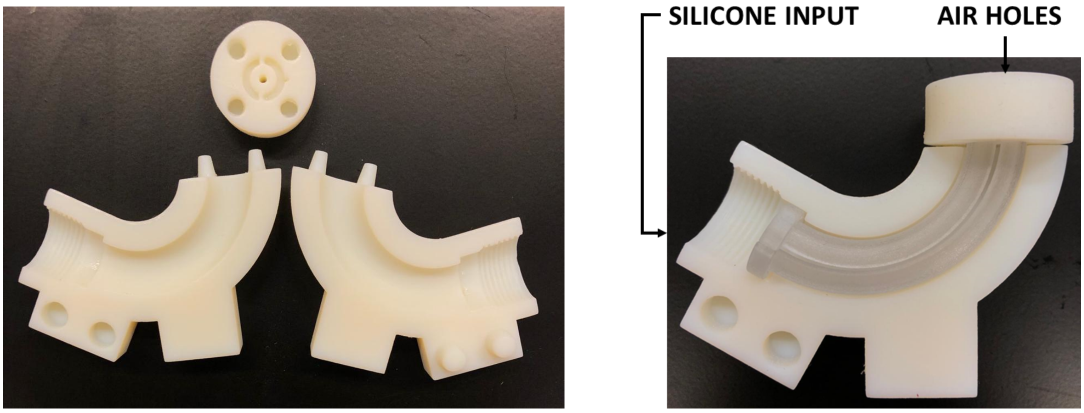

(a) **(b)**

Figure 4.3: Mould for the fabrication of the final design consisting of both the actuation chamber and the stiffening chamber. (a) depicts the outer mould and (b) depicts the integration of the moulds for the actuation chamber cavity and the stiffening chamber cavity placed within the outer moulds.

Once the actuator core has been cured, the cavity moulds are carefully removed. The open ends of the actuator core are closed my adding caps. The caps are added simply by dipping the open ends into a tub filled with liquid silicone, shown in Figure 4.4b. The tub has a diameter that is 0.1 mm larger than the diameter of the cured actuator core. The simplified preliminary design only has one open end after the first moulding step, while the final design has both ends uncapped. The final design, at this stage, has an outer diameter of 11 mm, shown in Figure 4.4a. Before adding the cap on the second end of the final design, the stiffening mechanism is inserted into the empty cavity. Once both ends of the module have been sealed, sharp needles are used to dig entry points for the pneumatic tubes.

(a) **(b)**

Figure 4.4: Addition of caps on either end of the actuator core. (a) depicts the diameter of the main body after de-moulding. (b) depicts the process of adding caps to the two open ends of the main body.

4.2 Shell-Reinforcement

The shell-reinforcement is a thin plastic sheet of 0.1 mm thickness that is laser-cut, as is shown in Figure 4.5a. The backbone and rings are formed when the sheet is curled onto itself such that the two strips holding the rings together are placed on top of each other and taped. This would result in the backbone being 0.2 mm thick while the rings have a thickness of 0.1 mm. The backbone strips are taped onto each other with double-sided tape. The large flaps at either end have been placed to make it easier to curl the sheet without damaging the rings. Once the shell-reinforcement has been prepared, it is carefully slid onto the module body. Since the shell-reinforcement should sit flush against the silicone module, vacuuming the inner cavities makes the process of sliding the shell-reinforcement into place much easier. Once the latter is in place, the extruding parts of the reinforcement are cut such that it sits flush with the end of the endoscope, depicted in Figure 4.5b.

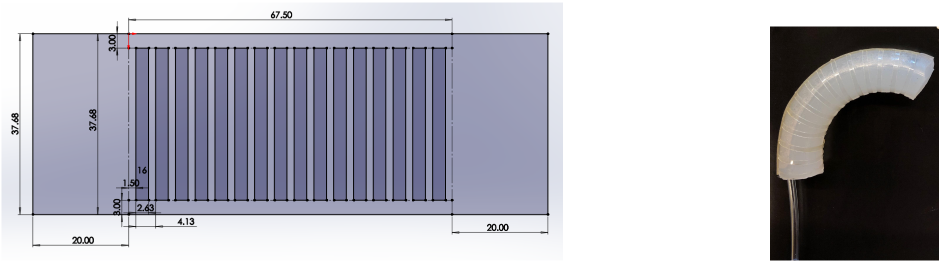

(a) **(b)**

Figure 4.5: Shell-reinforcement consisting of rings and a backbone. (a) depicts the drawing of the laser cut sheet and (b) depicts the shell-reinforcement added to the cured Ecoflex body.

4.3 Laminar Sheets

The laminar sheets are fabricated by laser cutting thin plastic sheets of 0.1 mm thickness into five strips. The dimensions of these are varied since the strips are to be inserted into the stiffening chamber which is located along the inner arc of the endoscope. This an be seen in Figure 4.6a. The jamming mechanism of the sheets is highly dependent on the friction between layers, therefore, the sheets are sanded down to increase the friction coefficient. Figure 4.6b depicts the endoscope after the implementation of the stiffening mechanism.

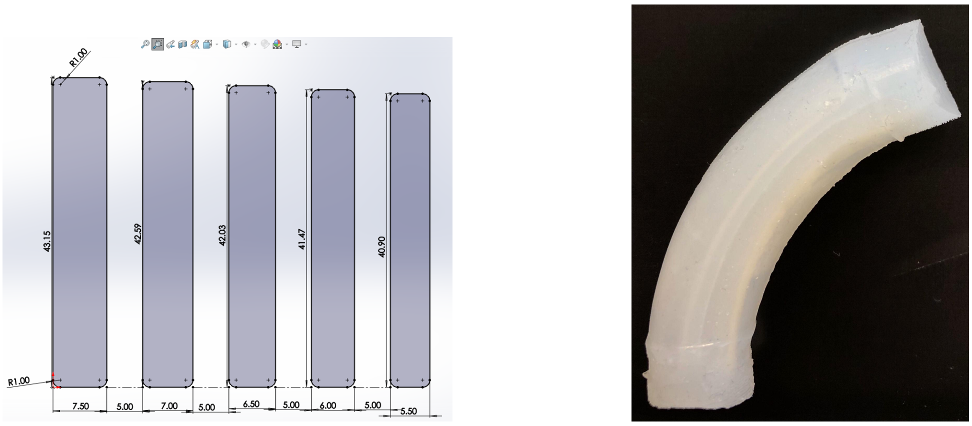

(a) **(b)**

Figure 4.6: Fabrication of the laminar jamming sheets. (a) depicts the CAD drawing of the sheets which are laser cut and (b) depicts the final endoscope with the sheets placed within the stiffening chamber.

4.4 Sheathing

The final step in the fabrication process is the addition of the sheathing. The module is fixed to a flat surface on one end as this makes its easier to slide the sheathing on. The maximum diameter of the external sheathing is specified to be 11 mm, however, in practice it is measured to be 12 mm. The 1 mm difference between the main body and the sheathing makes it easier to slide the sheathing on. The sheathing is fixed to the caps of the endoscope using Sil-Poxy^{TM} by Smooth-On, a silicone adhesive. The external sheathing is added such that along the inner arc, the fibre angle is as close as possible to zero degrees while along the outer arc the fibre angle is as large as possible. This follows the same orientation as the rings, which are closer together along the inner arc and farther away along the outer arc.

4.5 Discussion and Conclusion

The fabricated endoscopes do not meet some of the design parameters outlined in Table 3.4. The endoscopes are designed pre-bent, however, the maximum bending angle of the endoscope is not 120°, but around 90° instead. This is due to the influence of the stiffening mechanism and the shell-reinforcement. After the implementation of the stiffening mechanism, the maximum bending angle of the endoscope changes, as is depicted in Figure 4.6b. Since the laminar sheets are fabricated straight, when inserted into the empty chamber, they are compressed. Thus, acting like springs, they bend the endoscope module in the opposite direction and decrease its maximum bending angle.

The shell-reinforcement has a similar effect on the module. Additionally, the shell-reinforcement is not fixed to the body of the endoscope and therefore can move around. This is particularly difficult when adding the sheathing. As the sheathing is slid on, the rings move around and can bunch up leaving large exposed areas. This can be seen by the decrease in the diameter of the endoscope depicted in Figure 4.7b.

The addition of caps is an inconsistent process producing unique endoscopes. As can be seen in Figure 4.7a, the caps have been designed to stop at the indicated white line. However, due to the chosen fabrication process, in several prototypes, the caps exceeded the white line. In this case, the endoscope has a cap up to the red line. Therefore, the addition of caps is not properly controlled and can result in a decrease in volume of the actuation and stiffening chambers. For the same reason, the module lengths, which were designed to have an inner arc length of 50 mm with 5 mm caps, are not consistent between prototypes.

Finally, without the addition of the sheathing, the diameter of the endoscope is 11.2 mm. With the application of sheathing the diameter ranges from 12 mm-15 mm which is larger than the desired 12 mm.

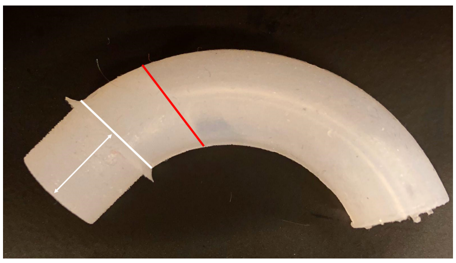

(a)

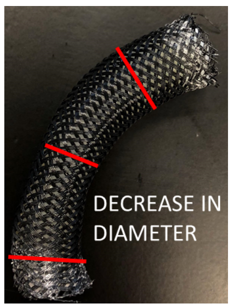

(b)

Figure 4.7: Errors in the fabrication process. (a) depicts the uncontrolled capping method decreasing the actuation and stiffening chambers. With the shell-reinforcement not fixed to the body of the endoscope, when adding the sheathing the rings can move, depicted in (b)

In conclusion, the design requirements met are the implementation of a stiffening mechanism, having a modular design, with lengths varying between 50 mm and 60 mm, decreasing the number of chambers to improve the scalability of the endoscope, a shell-reinforcement with 16 rings and a backbone width of 3 mm. The free central lumen is designed, however, it is not fabricated due to time constraints.

Table 4.1: Final design parameters compared to the fabricated endoscope.

Requirements	**Value**	**Fabricated**
Outer diameter	12 mm	12 mm - 15 mm
Module Length	60 mm	67 mm
Central lumen diameter	4.5 mm	n/a
Max bending angle	120°	90°
Stiffness	7.16 N/m - 0.28 N/m	n/a
Cross-sectional area - Actuation Chamber	$\frac{1}{2}$ of circumference	$\frac{1}{2}$ of circumference
Number of rings	16	16
Backbone Width	3 mm (15°)	3 mm (15°)
Laminar layers	5	5

5 Characterisation Experiments

In this chapter the performance of the final endoscope design outlined in Section 3.3 is presented and analysed. Two main experiments are performed, one captures the motion profile of the endoscope characterising the relation between the bending of the module with the applied pressure, that is, its bending performance, while the other characterises the stiffness of the module in the transverse and axial direction. Each experiment is performed with an inactive and active stiffening mechanism.

Approach:

The requirements yet to be met are the shifting of the dead zone, thereby improving the bending performance within the operating range (between 0° and 20°) and determining the effectiveness of the variable stiffening mechanism.

To determine whether the first design goal has been met, the bending performance of the final design is analysed. Additionally, the bending performance of the endoscope when the actuation and stiffening chambers are switched is also determined. This is done since improved performance was noticed during experimentation and testing.

The influence of the stiffening mechanism on the bending performance of the final design is determined by comparing the endoscope's bending performance with the simplified preliminary design. Additionally, the effectiveness of the variable stiffening mechanism is determined by measuring the stiffness when transverse and axial load is applied. Specifically, whether or not the endoscope tip can apply forces between 0.9 N to 3.3 N.

5.1 Experimental Set-Up

This section outlines the experimental set-up for the motion and stiffness characterisation experiments.

5.1.1 Motion Characterisation

Motion characterisation maps the relationship between the bending of the endoscope tip to the applied pressure. The experimental set-up for this is shown in Figure 5.1.

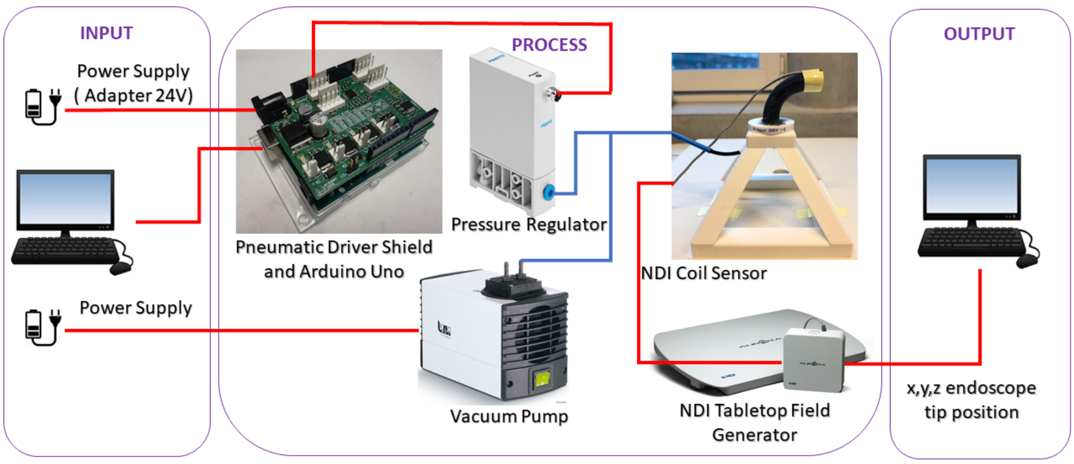

Figure 5.1: Experimental set-up for the motion characterisation experiments. All electrical signals are depicted in red while all pressure signals are depicted in blue.

The reference pressure for the actuation chamber ranges from 0 bar to 0.6 bar with increments of 0.005 bar. This positive input pressure is generated by the Proportional-Pressure Regulator

VEAB, part no. 8046307 (Festo, New Taipei City, Taiwan) in combination with the Arduino Uno REV3 and the pneumatic driver shield developed by Lenssen (2019). The main functionality of the shield is to deliver enough power to the regulator since the Arduino pins cannot supply the current required by the regulator. Voltages ranging from 0 V and 10 V are required and the shield amplifies the voltage from the Arduino by a factor of 2, as the maximum voltage provided by the latter is 5 V. Additionally, the shield can drive four pressure regulators at the same time (Lenssen, 2019).

The pressure regulator has a range from 0.005 bar to 1.0 bar with incremental steps of 0.005 bar. Although the pressure regulator can go up to 1.0 bar, a maximum pressure of 0.6 bar is applied to make sure the prototypes do not rupture or break. It is connected to the main pressure line and regulates the output pressure based on the input analogue voltage using an internal controller. The analogue voltage that is required by the internal controller to control the output pressure is provided by the Arduino and pneumatic driver shield via Pulse Width Modulation (PWM).

When needed, the stiffening mechanism is activated by de-pressurising the stiffening chamber using the Laboport Mini Diaphragm Vacuum Pump (KNF, New Jersey, USA). It can create a pressure difference of 0.12 bar below ambient pressure.

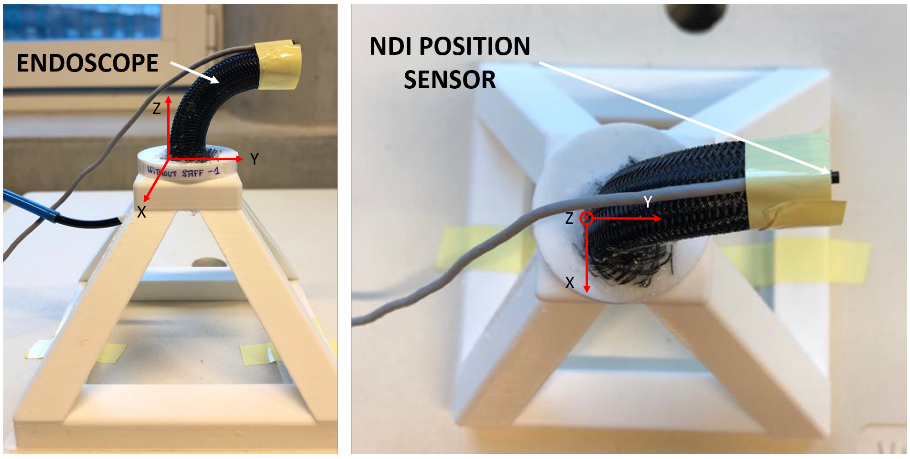

Figure 5.2: Experimental set-up of the endoscope on top of the NDI Aurora Tabletop Field Generator. On the left, the side view of the endoscope is depicted with the NDI sensor attached along the outer arc while the right depicts the top view.

The bending performance of the endoscope is measured using the NDI Aurora system (NDI Medical, Ontario, Canada). The NDI Aurora system consists of a tabletop field generator which emits low-intensity, varying electromagnetic field. The varying electromagnetic field generated by the tabletop induces small currents in the coil sensor, which are dependent on the distance and the angle between the sensor and the Field Generator. The Sensor Interface Units amplify and digitize the electrical signals from the sensor, and the Sensor Control Unit collects information from the Interface Unit. It calculates the position and orientation of the sensor and interfaces with the host computer. The endoscope is placed on the Aurora Tabletop Field Generator and the position sensor is attached to the tip of the endoscope along the outer arc, parallel to the backbone. For each experiment, the base of the endoscope is also measured, as it is required for data processing. The coordinate frame defined can be seen in Figure 5.2 along with the placement of the sensor on the endoscope.

5.1.2 Stiffness Characterisation

The stiffness characterisation maps the relationship between applied force and the displacement of the endoscope tip. The experimental set-up for this is shown in Figure 5.3.

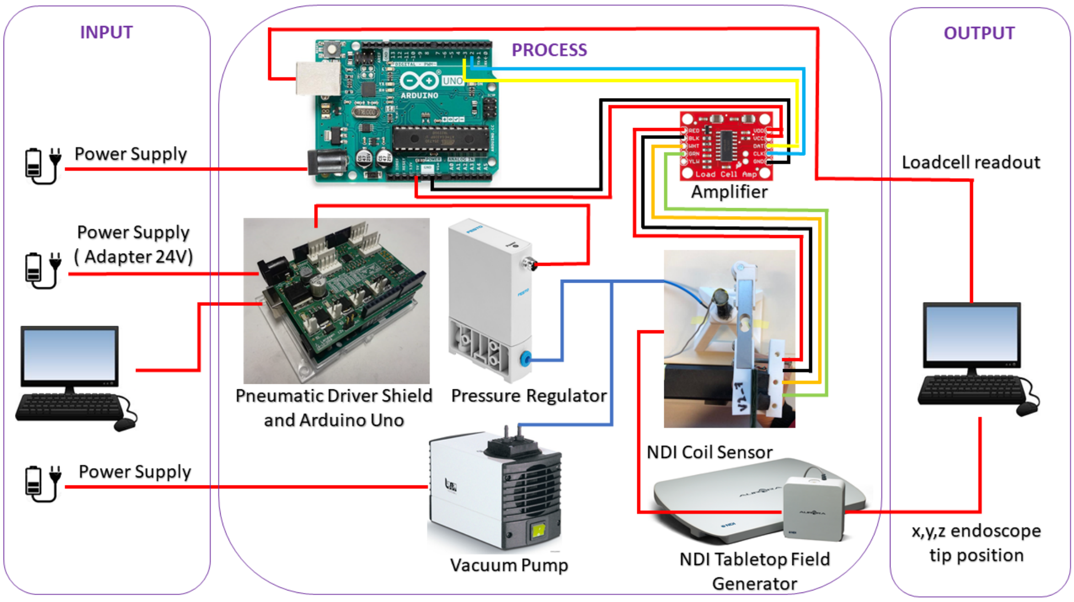

Figure 5.3: Experimental set-up for the stiffness characterisation experiments. All electrical signals are depicted in red while all pressure signals are depicted in dark blue. The electrical connections between the load cell, amplifier and the Arduino Uno are depicted with varying colours.

The experimental set-up for the stiffness characterisation is similar to the motion characterisation. The reference pressure set increases incrementally from 0 bar with steps of 0.005 bar bar till the endoscope is in an upright position, which is then maintained for the remainder of the experiment. The NDI Aurora System is used to track the displacement of the end-effector while the Load Cell - 10 kg, Straight Bar (TAL220) is used to apply pressure on the endoscope and read-out the reaction force. The load cell can translate up to 10 kg in pressure into electrical signals which are amplified with the SparkFun Load Cell Amplifier - HX711 and read-out by an Arduino Uno REV3. The digital signals read-out by the Arduino are converted to forces using load cell calibration.

5.2 Experimental Procedure and Data Processing

The experimental procedure and the data processing steps for both motion characterisation and stiffness characterisation experiments are explained below.

5.2.1 Motion Characterisation

Procedure The reference signal generation by the Arduino is set at a frequency of 2 Hz. Each experiment consists of the endoscope being pressurised and de-pressured four times, with the complete experiment taking 4840 sec. Pressurisation and de-pressurisation is the increasing and decreasing pressure of the actuation chamber. The NDI position sensor is sampled at a frequency of 40 Hz. The datasets from the NDI position sensor and the reference pressure signal are then synchronised, processed and presented in Section 5.3.1.

Data Processing The bending angle of the endoscope tip is calculated with the NDI position sensor data which is then synchronised with the reference signal generated by the Arduino. The manual synchronisation processes and the other data processing steps are explained in detail in Section A.1. The bending angle is calculated with the NDI sensor data and is plotted against the reference input pressure.

5.2.2 Stiffness Characterisation

Procedure The stiffness is determined in the transverse and the axial direction when the endoscope module is in the upright position, that is, at an angle of 0°. To determine the effectiveness of the stiffening mechanism, the measured stiffness in the transverse direction of the final design is compared with the simplified preliminary design, consisting of only the actuation mechanism. These experimental results are compared with the analytical results derived in Section 3.2.4. The locations of the transverse load applied along the circumference of the endoscope can be seen in Figure 5.4a.

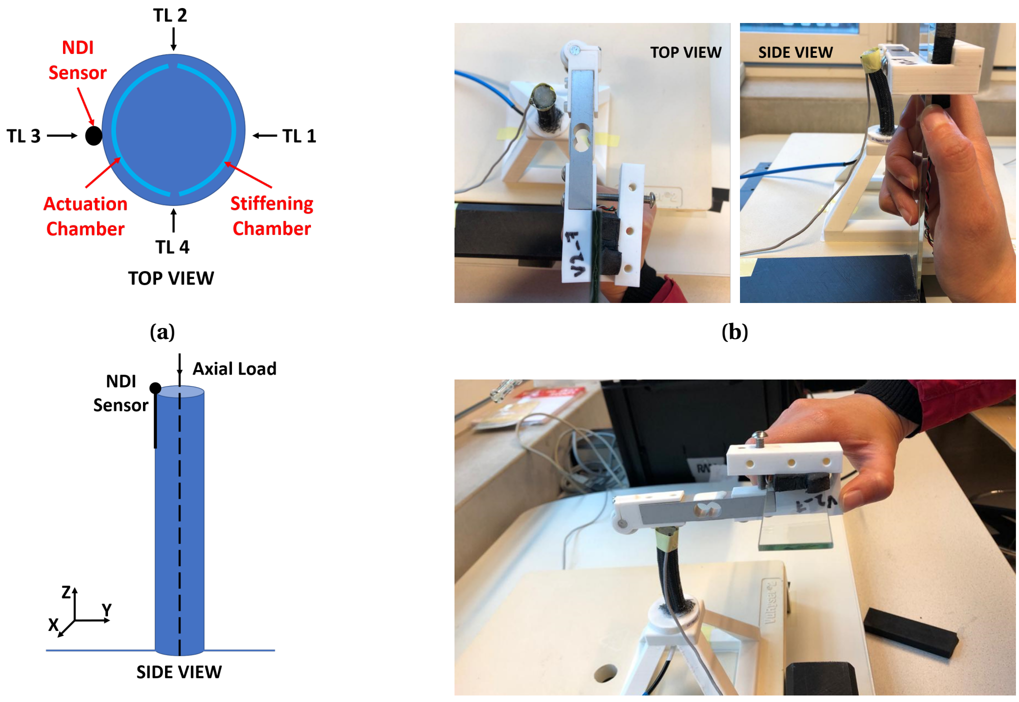

(c) (d)

Figure 5.4: Experimental set-up to determine the stiffness of the endoscopes with and without the activation of the stiffening mechanism. (a) depicts the application of transverse load in four directions around the circumference of the endoscope when in up-right position and (b) depict the load cell applying transverse load. (c) depicts the application of axial load and (d) depicts the load cell applying axial load.

For laparoscopy, the endoscope tip must be able to apply forces between 0.9 N to 3.3 N. Therefore, with uniaxial loading the maximum applied load before buckling is determined. This can be seen in Figure 5.4c. The application of the load cell for both experiments can be seen in Figure 5.4b and Figure 5.4d.

Each stiffness characterisation experiments is performed five times. Within each experiment the endoscope is displaced seven times, resulting in 35 datasets for each direction. The datasets from the load cell and the NDI position sensor are synchronised, processed and presented in Section 5.3.2.

Data Processing The process differs for transverse load and axial load experiments. For transverse load, both the NDI and load cell sensor data is used while for the axial load, only the load cell data is used. The two processes are explained in detail in Section A.2.

For transverse load experiments, NDI position and load cell sensor data, are synchronised. Additionally, the load cell is calibrated and the voltages measured are mapped to forces. The NDI position sensor data is used to calculate the bending angle. Once synchronised, the data sets are segmented such that only the data points corresponding to the positive displacement of the endoscope are plotted. Therefore, for each load, the reaction force measured by the load cell is plotted against the positive displacement. A linear curve is fitted through the data points as the stiffness in the linear elastic regime is of interest.

For axial load experiments, the point of buckling is determined by the point where the rate of change of the reaction force measured by the load cell has either decreased or is zero. The force at this point is measured and plotted.

5.3 Experimental Results

The results of both the motion characterisation and the stiffness characterisation experiments are shown below.

5.3.1 Motion Characterisation

The motion profile of the final design with and without the activation of the stiffening mechanism can be found in Figure 5.5. Similar to the experimental results from Lin (2019), shown in Chapter 1, there is a start-up transient with a dead zone that lasts up to an applied pressure of 0.015 bar followed by non-linear bending motion till 0.02 bar. The rest of the bending motion is linear. The endoscope starts at an angle of approximately 85.5°.

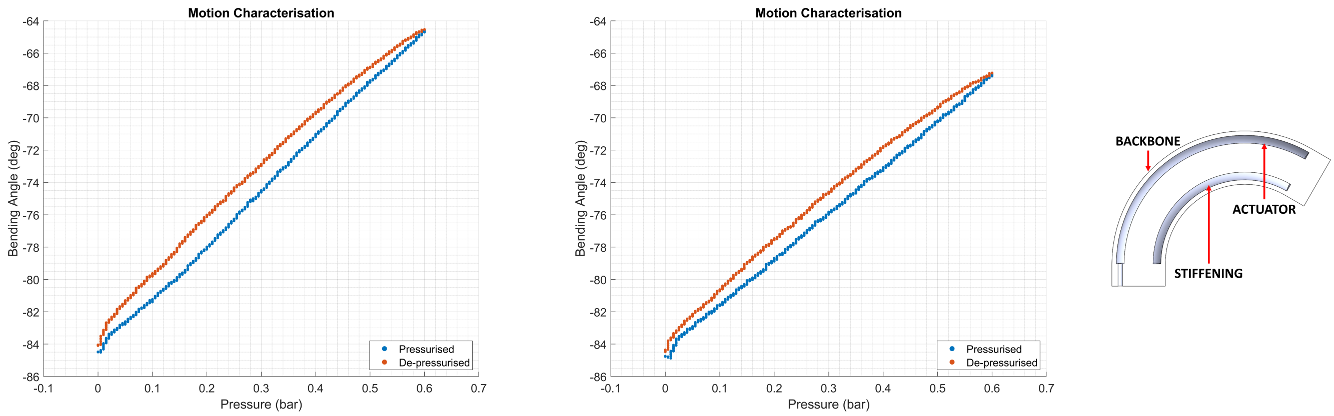

(a) (b)

Figure 5.5: Bending performance of final design with (a) inactive and (b) active stiffening mechanism.

In Figure 5.5a and Figure 5.5b, the maximum bending angle of the endoscope is $-65.5°$ and $-67.5°$ respectively. It should be noted that with an inactive stiffening mechanism, the endoscope reaches a higher final bending angle compared to an active stiffening mechanism. The difference in final position is approximately 2°.

The hysteresis for this endoscope is much lower compared to that of Lin's endoscope. In this design there is a variation of approximately 2.5° between pressurised and de-pressurised motion, which is approximately 12° lower than Lin's endoscope.

Additional influence of the stiffening mechanism on the bending performance is seen by comparing its motion profile with that of the simplified preliminary design, which consists of only the actuation chamber. This is depicted in Figure 5.6.

There is a start-up transient between 0 bar and 0.08 bar with a dead zone up to 0.01 bar. Following that, from approximately 0.08 bar to 0.32 bar, the motion profile of the endoscope is mostly linear. After 0.32 bar the profile is once again non-linear. There is hysteresis between pressurised and de-pressurised motion with a maximum variation in bending angle of approximately 7.5°. The endoscope reaches an upright position, that is, bending angle of 0°, at an applied

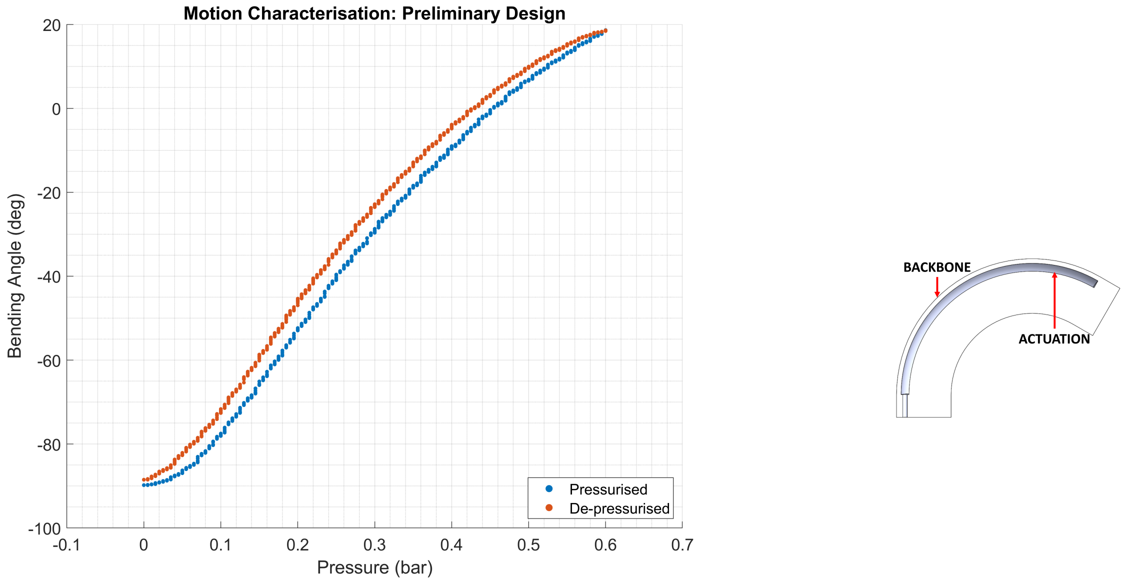

Figure 5.6: Bending performance of the simplified preliminary design.

pressure of 0.46 bar when pressurised and 0.44 bar when de-pressurised. At near-straight configuration the motion of the endoscope is non-linear.

Discussion

The motion profile of the final design is severely constricted compared to the simplified preliminary design. In the case of both inactive and active stiffening mechanism, the endoscope does not bend more than 20° from its initial position, and therefore does not reach an upright position. This is because when the actuation chamber is pressurised, it constricts the stiffening chamber resulting in the contact and subsequent increase in static friction between the laminar jamming sheets. This inadvertently activates the stiffening mechanism. This can be countered by pressurising the stiffening chamber containing the jamming structure such that the laminar sheets are kept from interlocking. The drawback with this method is that when stiffening is activated, the pressurised stiffening chamber must be de-pressurised resulting in the endoscope tip changing position. Another method to counter the de-pressurisation of the stiffening chamber when the actuation chamber is pressurised is by making sure that the wall in between the two chambers is stiffer. This would increase the overall stiffness of the endoscope.

The performance of the endoscope when the stiffening chamber is pressurised showed improved bending performance. This can be seen in Figure 5.7.

Three phases can be identified: the start-up transient motion, the linear motion and finally the transient non-linear motion at the end. Unlike the final design, this endoscope has a significant dead zone in the beginning, lasting till approximately 0.06 bar. Following the dead zone, the bending motion is non-linear till approximately 0.12 bar after which it is linear till 0.22 bar. A bending angle of 0° is obtained at a pressure of 0.18 bar when pressurised and 0.14 bar when de-pressurised. Therefore, this endoscope has linear motion around the operating region. Further more, the range of motion is large compared to other design configurations, from $-70°$ to 110°. Although this is not a requirement for this design, it can be advantageous. The hysteresis, however, is large compared to other design configurations, with a maximum variation in bending angle of 40°.

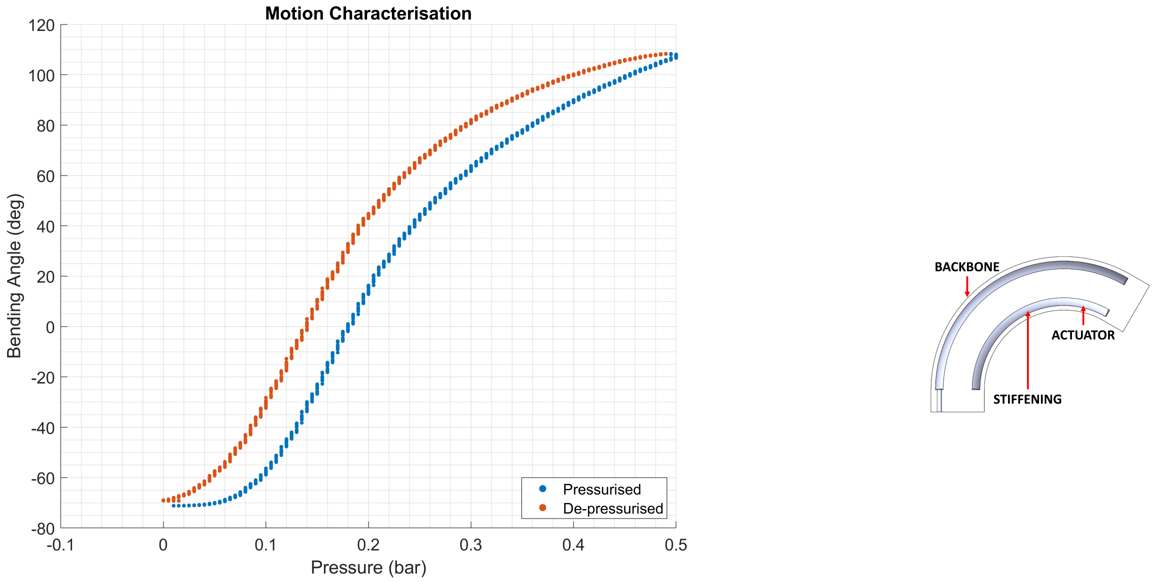

Figure 5.7: Bending performance of final design with pressurisation of stiffening chamber.

The improved performance of the endoscope is due to the presence of the laminar sheets within the stiffening chamber. The sheets help the endoscope straighten since they are essentially, compressed springs when the endoscope is at rest in a bent position.

Another factor influencing the bending performance is the location of the actuation chamber. The motion profile of an endoscope with two empty chambers, one along the inner arc and one along the outer arc, is determined when either of the chambers is actuated. This is depicted in Figure 5.8.

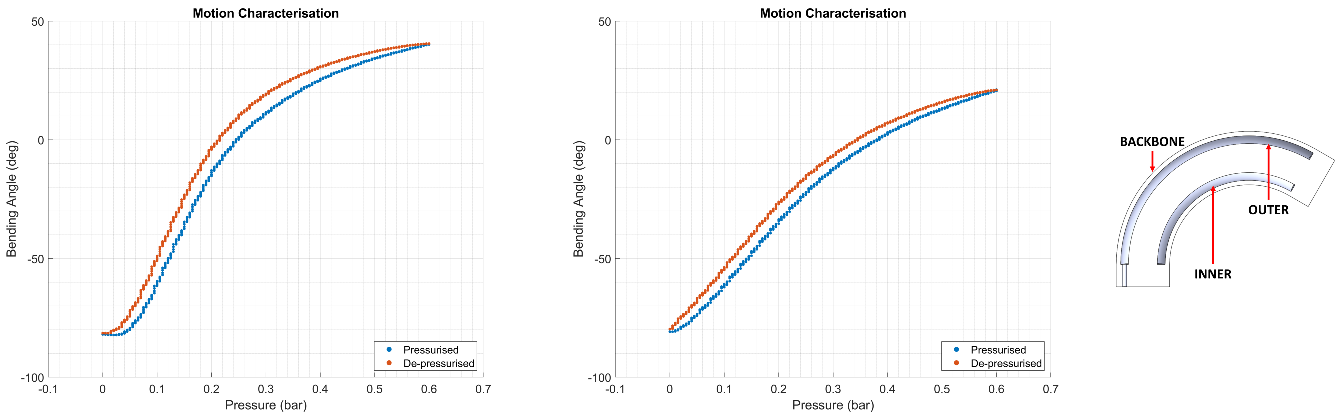

(a) **(b)**

Figure 5.8: Bending performance of endoscope with empty chambers along the (a) inner and (b) outer arc.

Here it can be seen that the endoscope reaches a maximum bending angle of 40° when actuating the inner chamber. When actuating the outer chamber, the endoscope reaches a maximum bending angle of 20° for the same input pressure of 0.6 bar. Actuating the inner arc results in the endoscope reaching upright position with an input pressure of 0.24 bar while an input pressure of 0.32 bar is required to reach an upright position when the outer arc is actuated. Thus, the performance of the endoscope is significantly improved when the actuation chamber is along the inner arc. A larger bending angle for a lower input pressure is desirable as it is safer for use within the human body.

Unfortunately, neither of the two are linear within the operating range, There is also a significant dead zone present when actuating the inner chamber. This is not the case when the outer chamber is actuated, which is to be linear from the start. Similar to Figure 5.7, the dead zone seems to be attributed to actuating the inner chamber. The hysteresis present in both is below 10° between pressurised and de-pressurised motion.

Based on the results shown in Figure 5.8, the final design is updated by switching the actuation and stiffening chambers. The actuation chamber is along the inner arc while the stiffening mechanism is along the outer arc. The motion profile of the design with the switched chambers can be found in Figure 5.9. The motion profile when the stiffening mechanism is inactive and active are shown in Figure 5.9a and Figure 5.9b, respectively.

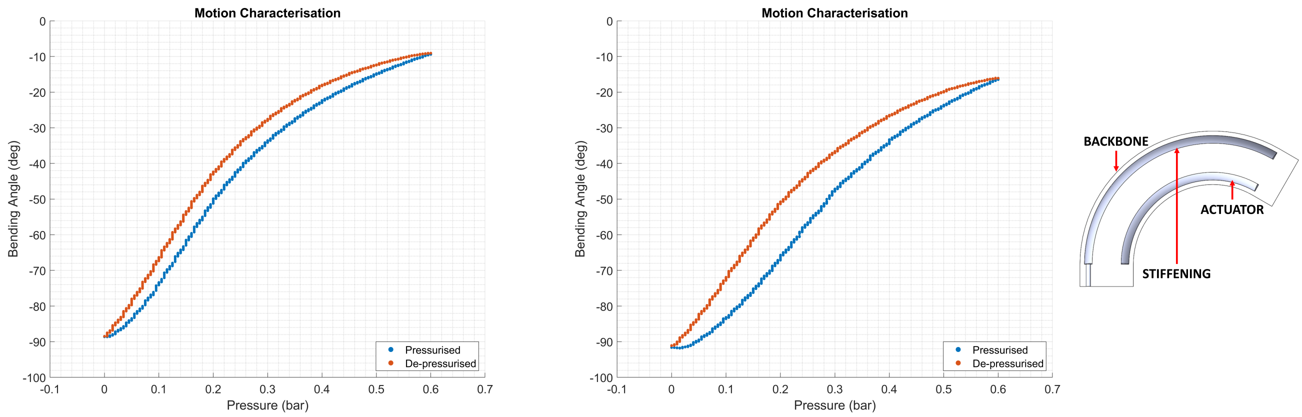

(a) (b)

Figure 5.9: Bending performance of endoscope with switched chambers for (a) inactive and (b) active stiffening mechanisms.

In both cases the endoscope bends significantly further than the final endoscope design, where the maximum bending angle was −65.5°. Here, the endoscope has a maximum bending angle of −10° when the stiffening mechanism is inactive and −16° when the stiffening mechanism is active. The hysteresis present in the latter is larger than the former, with a variation of 14° compared to 10° respectively.

The motion profiles of the switched chambers, with and without the actuation of the stiffening mechanism, have a dead zone that lasts till 0.03 bar and 0.01 bar respectively. This dead zone is five times smaller than the one observed in Lin's work. This is due to the addition of rings. Much like Lin's design, the final endoscope is encased in a sheathing resulting in a gap between the endoscope body and the inner circumference of the sheathing. However, with the rings attached directly to the body of the endoscope, it begins to move immediately when pressurised. The reason for this is that the rings limit the radial expansion immediately. Regardless, the advantage of the pre-bent endoscope is that the non-linear start up transient is well out of the operating range.

Compared to Figure 5.9a, the hysteresis seen in Figure 5.9b is significantly larger, with a variation in bending angle of 14°. This is because the activation of the stiffening mechanism increase the static friction, which increases the dead zone, lasting till 0.03 bar. When pressurising from the rest position, the static friction due to the stiffening mechanism is larger than the dynamic friction when de-pressured, which is represented as the dead zone at 0.005 bar in Figure 5.9b.

Similarly, the hysteresis seen in Figure 5.7 is large compared to other experimental results, with a maximum variation of 40°. The large variation can be attributed to static friction, which is also larger. This can be seen by the dead zone which lasts up to 0.06 bar, which is six times larger than the design where the actuation and stiffening chambers are switched. The difference is the placement of the stiffening mechanism. Therefore, the reason for the larger dead zone and hysteresis can be attributed to the increased compression of the jamming structure when placed in the inner cavity compared to the outer cavity, thereby increasing the static friction.

Conclusion

The motion characterisation experiments show that the proposed design has shifted the dead zone out of the operating range. Compared to the performance of the final design, the endoscope with the switched chambers bends farther, however, it does not reach an upright position and has non-linear motion in the operating range. Further more, the hysteresis of the switched chambers design with an inactive stiffening mechanism is less than that compared to Lin's endoscope which has a maximum variation in bending angle of approximately 15°.

5.3.2 Stiffening Characterisation

The stiffening characterisation experiments performed are subdivided into stiffness in the transverse and axial direction. The results for these are explained below.

Transverse Load

The stiffness characterisation experiment results in the transverse direction of the endoscope with the switched chambers is depicted in Figure 5.10. The experiment was not performed on the final model since its motion profile is limited and it is unable to reach near-straight configuration. Figure 5.10a and Figure 5.10b depict the stiffness in all four directions with an inactive and active stiffening mechanism, respectively.

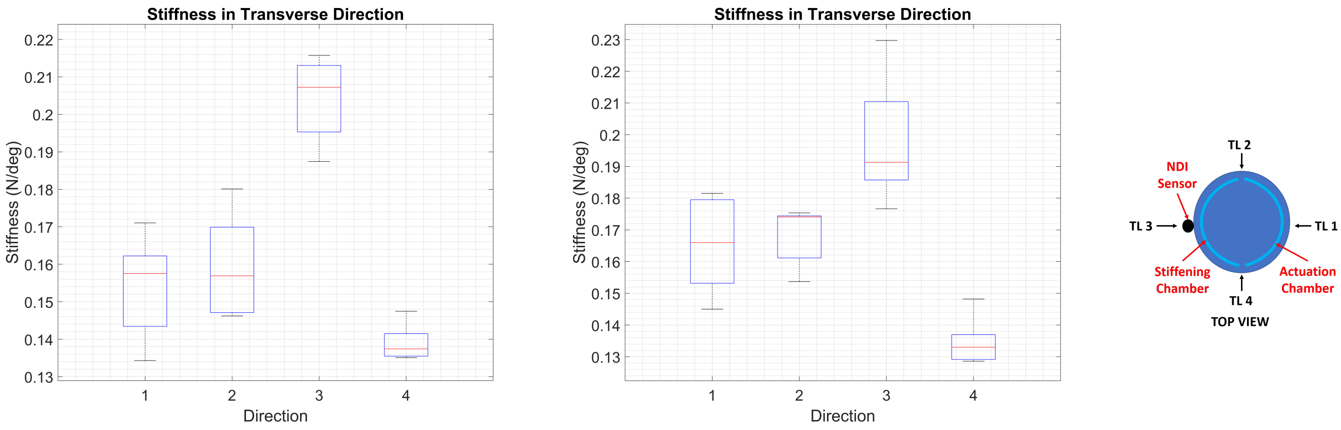

(a) (b)

Figure 5.10: The stiffness characterisation in transverse directions of the endoscope with switched chambers for (a) inactive and (b) active stiffening mechanism.

The box plot depicted, shows that there are large deviations in the stiffness in most transverse directions. Since the endoscope is designed such that it is symmetric along the central axis, the stiffness measured at TL2 and TL4 should be similar while the stiffness in TL1 and TL3 should differ. In both situations, with and without the activation of the stiffening mechanism, TL2 and TL4 are not similar.

In Figure 5.10a, the stiffness in TL1 and TL2 is similar, with a median stiffness of 0.158 N/deg and 0.157 N/deg respectively. The largest stiffness is in TL3 with approximately 0.208 N/deg while the lowest is in TL4, with median stiffness of 0.136 N/deg. The difference between the upper and lower quartile is the least for TL4, with larger deviations noticed the other three.

In Figure 5.10b, the stiffness in TL1 and TL2 is similar, with a median stiffness of 0.166 N/deg and 0.175 N/deg, respectively. Here, the stiffness in TL2 is larger with a smaller difference between the upper and lower quartile. The median for the latter is located right next to the upper quartile indicating that the data is skewed towards the upper quartile. Further more, the limits of the box plot for TL1 compared to those in Figure 5.10a are shifted towards higher stiffness.

Similar to Figure 5.10a, the largest stiffness is in TL3, with a median of 0.192 N/deg while the lowest is in TL4, with a median stiffness of 0.134 N/deg. In both cases, the stiffness has decreased with the activation of the stiffening mechanism. The limits of the box for TL3 increases in Figure 5.10b compared to Figure 5.10a with the data skewed towards the lower limit.

Based on the results seen in Figure 5.10, difference in the stiffness of the endoscope when transverse load is applied, with and without the activation of the stiffening mechanism, is limited. The effect of the stiffening mechanism on the stiffness of the endoscope is determined by comparing the stiffness in the transverse direction of the switched chambers endoscope with the simplified preliminary design that consists of only the actuation mechanism. Therefore, the lower limit of the stiffness is determined. The result of this is depicted in Figure 5.11.

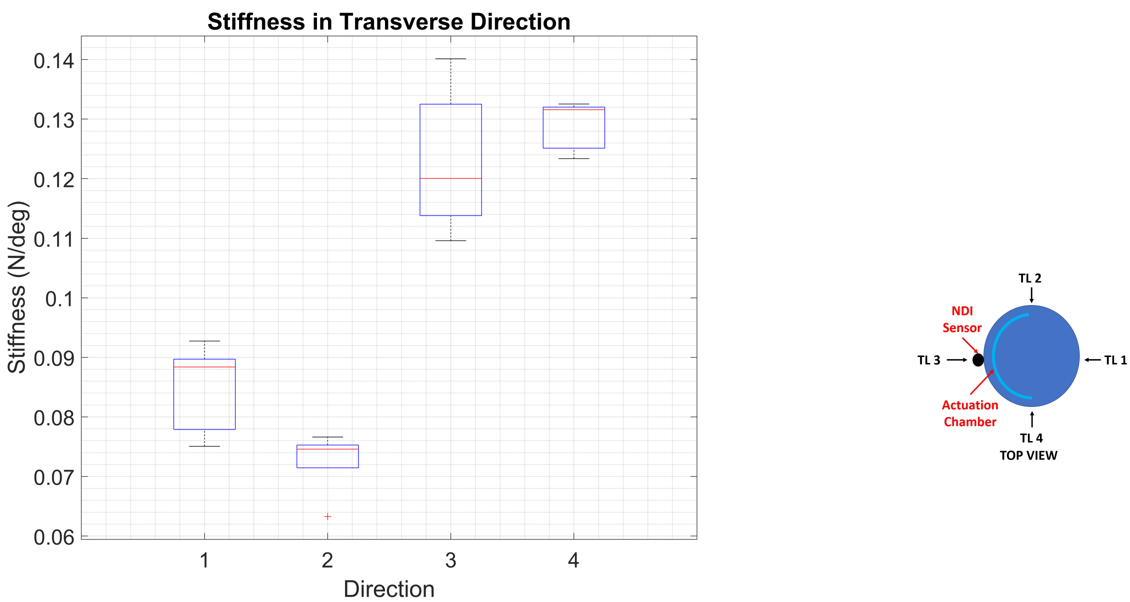

Figure 5.11: The stiffness characterisation in transverse directions of the simplified preliminary design only consisting of the actuation mechanism.

Here, the complete range of stiffness in all directions is between 0.062 N/deg and 0.14 N/deg. This is significantly lower than with the implementation of the stiffening mechanism, which has a range of 0.128 N/deg to 0.230 N/deg. Interestingly, the largest stiffness is in TL4 while the lowest is in TL2. This is contradictory to what is expected. There is a singular outlier in TL2 with the majority of the data skewed towards the upper quartile. This is also the case for both TL1 and TL4. TL3 has the largest difference between the upper and lower quartile.

Discussion and Conclusion

The simulation results of the analytical model, outlined in Section 3.2.4, depicted a minimum stiffness of 0.28 N/m and a maximum stiffness of 7.16 N/m. The model is of a jamming structure behaving like a cantilevered beam with a fixed end and a distributed load applied. Therefore, the transverse load in TL3 direction matches model. The experimental results show that the stiffness in TL3 direction for the switched chambers and the simplified preliminary design is 0.208 N/deg and 0.120 N/deg. The analytical model is an over-estimation of the stiffening mechanism and does not represent real world performance. This can be because the elastic modulus of the laminar sheets used in the analytical model is an estimation and does not represent the sheets used in fabrication.

For all experiments, there are large deviations in the data. A source of error is the data processing methodology. As explained above, data processing consists of synchronizing the datasets from the NDI position sensor and the load cell. Both sensors operate at a different frequency and interface with different hosts. Therefore, the manual process of syncing the two datasets results in inaccuracies that are reflected in the results. Since both datasets are plotted against each other, any shift in time will affect the results.

Further more, the experimental set-up adds various inaccuracies. As can be seen in Figure 5.4, the load cell is fixed onto a vertical slab which is moved to apply transverse and axial load to the endoscope tip. This motion is prone to several sources of error, such as uncontrolled point of contact between the load cell and the endoscope tip. The vertical slab, which is meant to keep the load cell steady, is not effective and the load cell does not apply force at the same point in the same orientation. Slight changes in the angle and location of the load cell can affect the load cell data.

Additionally, the dynamic response of the pressure regulator can also influence the data by adding low-frequency noise. Although the motion of the load cell is kept steady and slow, to get quasi-static motion, unintentional jerky movement will excite the system, thereby making the dynamic response of the pressure regulator apparent. The response can also be a delay due pressure tube lag.

Although the endoscope has been designed such that it is symmetric along the central axis, the stiffness in TL2 and TL4 is not similar. This is due to fabrication errors. As mentioned in Chapter 4, the fabrication process currently does not produce consistent endoscopes, leading to inaccuracies that can effect the symmetry of the design.

The bending stiffness of the endoscope with switched chambers is higher than that of the simplified preliminary design. Therefore, the implementation of the stiffening mechanism increased the base stiffness of the endoscope. The bending stiffness in TL3 is largest because the transverse load applied is opposite to the bending direction. The placement of the rings along the inner arc also inhibits the bending of the endoscope when the transverse load is applied. Therefore, when the actuation chamber is pressurised, the rings, which were in close contact, spread farther away from each other as the endoscope straightens and the actuation chamber balloons until it come in contact with the sheathing. The ballooned parts of the actuation chamber add stiffness when TL3 is applied.

The variation in bending stiffness when the stiffening mechanism is activated compared to when it is inactive is small. There is a slight increase in stiffness for the former. This is because the stiffening mechanism is constrained whenever the actuation chamber is pressurised. Therefore, by activating the stiffening mechanism there is a very small difference in stiffening because it was inadvertently already activated. To measure the true variation in stiffness between the active and inactive stiffening mechanism, the stiffness characterisation experiments must be performed when the actuation chamber is not pressurised and the endoscope is at rest.

Axial Load

Figure 5.12 depicts the maximum axial load the endoscope can withstand before buckling. Here, the load for the simplified preliminary design and the switched chambers endoscope with and without the activation of the stiffening mechanism is shown. The simplified preliminary design can withstand the lowest axial load, with a median force of 1.410 N. The switched chamber with an inactive stiffening mechanism can withstand a force of 2.190 N and with an active stiffening mechanism, the endoscope can withstand 2.775 N. The difference between the upper and lower quartile of the datasets is largest for the switched chambers with an active stiffening mechanism while it is lowest for the simplified preliminary design.

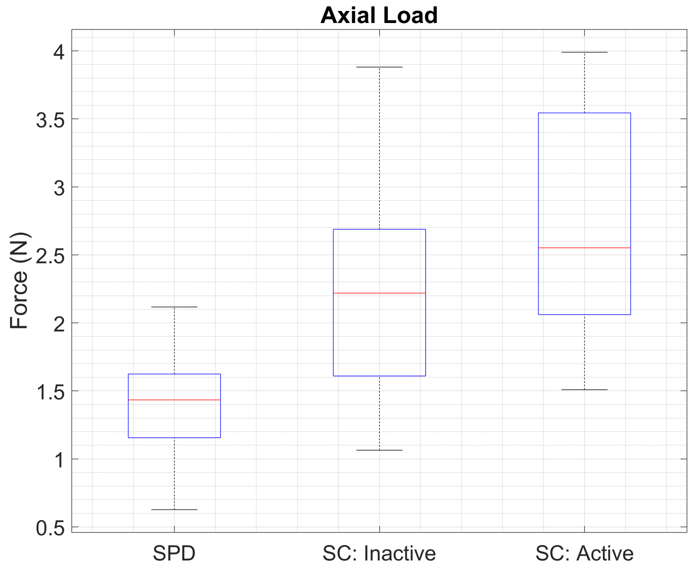

Figure 5.12: Axial load before buckling. *SPD* is the Simplified Preliminary Design and *SC* is the switched chamber endoscope with inactive/active stiffening mechanism.

Discussion and Conclusion

The maximum axial load that the endoscope can withstand is within the desired range of 0.9 N and 3.3 N. However, the data consists of large variations which are due the inconsistencies in the datasets. Similar to the transverse stiffness experiments, the variations can be attributed to the dynamic response of the pressure regulator. Further more, there is limited control over the orientation and the location of the applied axial load with the load cell. The data processing performed is manual, where each dataset is observed and the point of buckling is manually determined, introducing additional sources of error.

Based on the results shown in Figure 5.12, the force applied by the endoscope ranges between 1.4 N to 2.7 N which is within the acceptable range of applied force for endoscopes capable of performing laparoscopy.

6 Discussion and Conclusion

In this section, the research is discussed based on the design goals and research objectives. The thesis is then concluded and recommendations for further research are outlined.

The research has focused on developing a novel endoscope capable of performing laparoscopy. It aimed at improving the bending performance and implementing variable stiffening mechanism so that the endoscope can apply the forces required during medical intervention. Several design goals and research objectives were determined and they are discussed below:

Design goal: Shift dead zone such that bending performance is within the limits of laparoscopy.

The motion characterisation experiments show that the dead zone is shifted out of the operating range region. Therefore, finer control over the endoscope's angle within the operating range can be achieved by beginning in a pre-bent position. Additionally, the size of the dead zone is decreased with the implementation of the inextensible rings. The bending performance could be further improved by having linear motion at near-straight configuration. This was however, not possible. Most motion profiles exhibited non-linear motion at near-straight configuration while those with the stiffening mechanism implemented were unable to straighten up entirely. This is because with the current design, the stiffening mechanism is inadvertently activated whenever the actuation chamber is pressurised. Therefore, although the dead zone is shifted, the endoscopes with stiffening mechanism were unable reach near-straight configuration, requiring further development to be applicable for MIS.

Design goal: Improve space allocation for scalability of the endoscope.

Improving the scalability of the endoscope is important for modular design and future development. The scalability of the endoscope is improved by decreasing the number of chambers from three to two. This reduces the space required for pneumatic tubes when the modules are stacked. The disadvantage, however, is the limited DOF of the endoscope. The endoscope only has one degree of motion and would require an additional actuation method, such as rotation of the base, to get a larger range of motion. The additional actuation method in combination with the current design would result in a singularity at the near-straight configuration.

Research objective: To identify design parameters that influence the bending performance of the endoscope

Several design parameters that influence the performance of the endoscope were determined using FEA and analytical modelling. For the actuation mechanism, the cross-sectional area of the actuation chamber directly influences the bending moment of the endoscope. The number of rings effects the amount of the ballooning and therefore the point of failure of the endoscope. Finally, the width of the backbone influences the performance of the endoscope as a larger backbone results in a stiffer endoscope which limits the bending range. For the stiffening mechanism, the number of sheets implemented is directly proportional to the stiffness of the jamming structure.

Research objective: To identify how effective laminar jamming is as a variable stiffening mechanism.

To be applicable for laparoscopy, the endoscope must be able to exert forces between 0.9 N to 3.3 N. Based on the stiffening characterisation experiments performed, the forces exerted by the endoscope tip range from 1.4 N to 2.7 N. 1.4 N is the maximum axial load sustained by the simplified preliminary design while 2.7 N is the maximum axial load sustained by the endoscope with the switched actuation and stiffening chambers. The latter is when the stiffening mechanism is activated. The difference in force between active and inactive state is

0.6 N whereas between inactive switched chambers endoscope and the simplified preliminary design is 0.7 N. The difference in both can be attributed to the inadvertent activation of the stiffening mechanism when the actuation chamber is pressurised. Additionally, in the second case the addition of the stiffening mechanism in the switched chambers endoscope influences the maximum load that the endoscope can sustain. Regardless, the range of forces applied by the endoscopes is within the desired range.

Further more, the stiffness characterisation performed in the transverse direction shows that the difference in the stiffness, with and without the activation of the stiffening mechanism, is smaller than expected. Once again, this can be attributed to the inadvertent activation of the stiffening mechanism when the actuation chamber is pressurised. Therefore, the complete range of stiffness when transverse load is applied for the switched chambers endoscope cannot be determined from the characterisation experiments performed.

In conclusion a novel soft-surgical endoscope had been designed using soft pneumatic actuation system with added variable stiffening mechanism to improve the bending performance and functionality for MIS applications. It is shown that the performance of the endoscope compared to previous work has improved, specifically with a successful shift of start-up behaviour out of operating range. The variable stiffening mechanism is shown to increase the stiffness of the endoscope, however it limits the bending range and its implementation needs to be further investigated.

6.1 Recommendations

Several recommendations can be made to improve and further develop the novel endoscope presented in this thesis. They are:

- *Stiffening Mechanism*: The current implementation of the stiffening mechanism interferes with the bending performance of the endoscope. Improvements in the implementation or even the choice and design of the variable stiffening mechanism must be made such that the stiffening mechanism is not influenced by the pressurisation of the actuation chamber. For example, development as a miniaturised segment locking structure.
- *Fabrication Process*: The fabrication process directly impacts the performance of the endoscope and needs to be further refined. The current process, is riddled with manufacturing inaccuracies and the largest improvement can be made by streamlining the design of the caps. Additionally, the possibility of 3D printing the entire endoscope for added precision can be investigated.
- *Additional DOF*: Currently available endoscopes have the ability to bend in all directions whereas the novel design has one DOF. The range of motion of the endoscope can be drastically increased by adding a second DOF. This will improve the functionality of the endoscope and enable surgeons to manoeuvre around organs and reach difficult surgical targets. An additional DOF can be added by designing a rotating base.

A Data Processing

The data processing is different for motion characterisation and the stiffness characterisation experiments. Both of these will be outlined in detailed below.

A.1 Motion Characterisation

Motion characterisation determines the bending performance of the endoscope. It is the bending angle of the endoscope tip for an input pressure. The input reference pressure is generated by the arduino at a frequency of 2 Hz, while the NDI position sensor, placed at the endoscope tip, samples at a frequency of 40 Hz. An example of the raw data can be seen in Figure A.1.

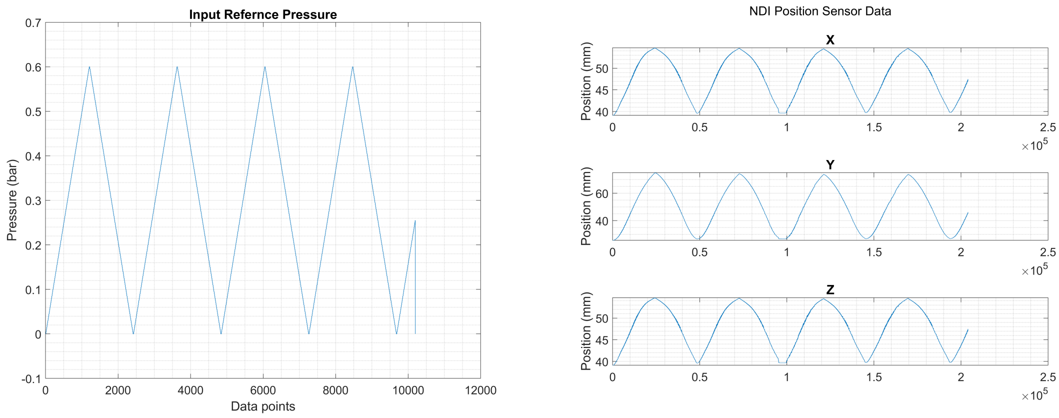

(a) **(b)**

Figure A.1: The raw datasets of the reference pressure generated by the (a) arduino and the (b) NDI position sensor.

High frequency noise is filtered out of the NDI position sensor data and the bending angle is calculated, as explained in Section 3.2. This can be seen in Figure A.2. The two datasets are synchronised by mapping the NDI data points that correspond to the arduino data. As the arduino generates a signal at 2 Hz, every 20^{th} NDI data point corresponds to the arduino data, assuming the arduino generates a reference pressure at equal time steps.

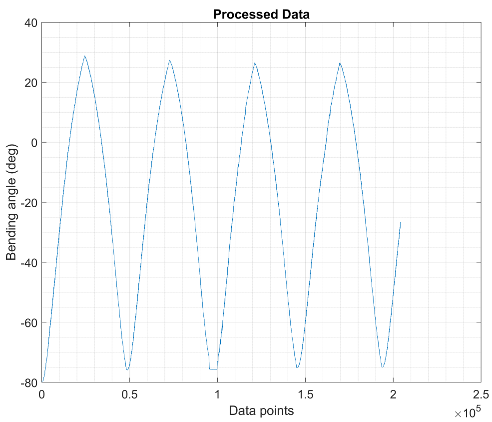

Figure A.2: NDI sensor data filtered and processed to represent the bending angle.

The synchronised data sets are plotted against each other to produce the figures in Section 5.3.1.

A.2 Stiffness Characterisation

The stiffness characterisation experiments undergo different processing. For transverse load, both the NDI and load cell sensor data is used while for the axial load, only the load cell data is used.

Figure A.3 depicts the raw NDI and load cell sensor data. As mentioned in Section 5.2, the stiffness characterisation experiments in the transverse directions are performed seven times and the two dataset are synchronised manually. The load cell samples at a lower frequency compared to the NDI position sensor and the data is interpolated.

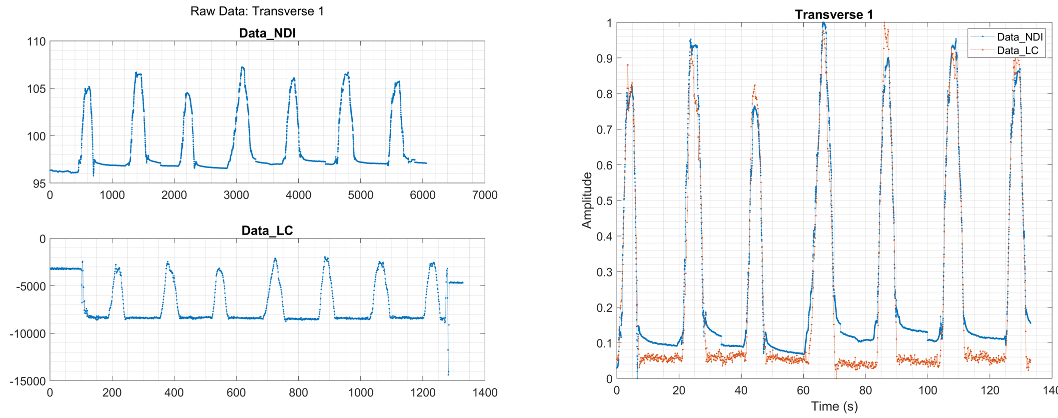

(a) **(b)**

Figure A.3: The raw datasets of the (a) NDI position and load cell sensor. (b) manually matched datasets.

The correlation of the synchronised data, depicted in Figure A.4a, shows that the datasets are synchronised. To determine the stiffness, which is the gradient of the force and displacement curve, the load cell is calibrated to map the readout to a force. The load cell is calibrated with fixed weights, shown in Figure A.4b.

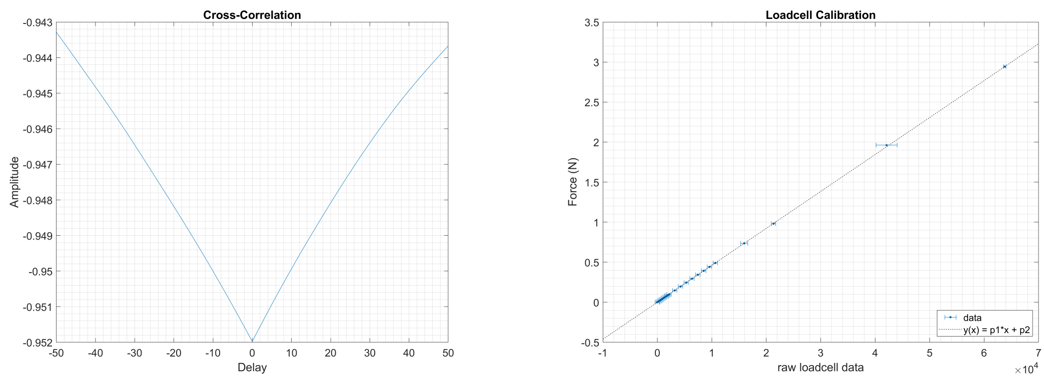

(a) **(b)**

Figure A.4: The cross-correlation between the load cell and the NDI sensor data shown in (a) while (b) is the calibration of the load cell.

As the characterisation experiment is performed seven times, the positive slope of each experiment is measured by segmenting both the NDI and load cell data. This segmented data can be seen in Figure A.5. A linear curve it fitted through the data to determine the stiffness in the linear elastic regime. The stiffness in all transverse directions are measured and plotted in Figure 5.10.

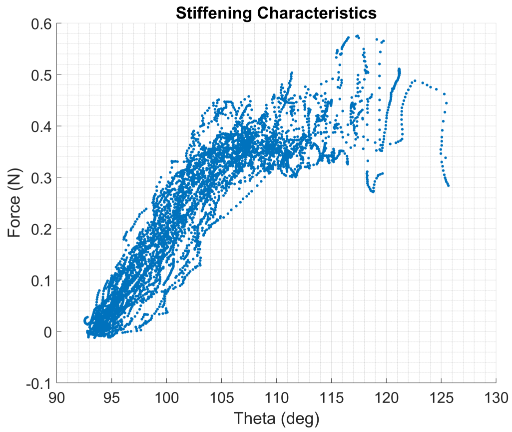

Figure A.5: Segmented data from the NDI and load cell, plotting all positive slopes from experiments performed with transverse load in TL1 direction.

For the axial load experiments, only the load cell sensor data is used to determine the maximum force applied by the endoscope tip. This is done by identifying the point of buckling, which is where the rate of change of the reaction force measured has either decreased or is zero. This can be seen in Figure A.6, where the point of buckling is at data point 20 and corresponds to an axial load of 2 N. The force at this point is measured and plotted for all datasets and shown in Figure 5.12.

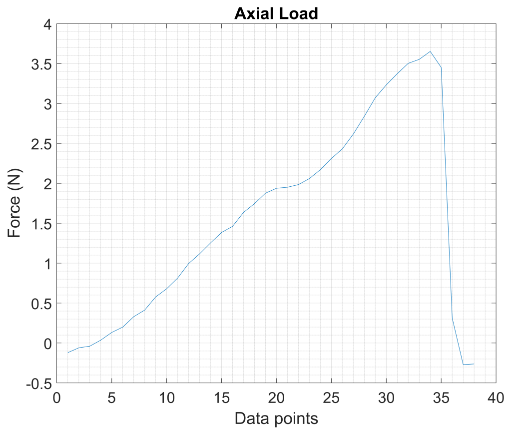

Figure A.6: Load cell sensor data for axial load experiments. The point of buckling can seen by the decrease in the rate of change of the reaction force.

Bibliography

Abidi, H., G. Gerboni, M. Brancadoro, J. Fras, A. Diodato, M. Cianchetti, H. Wurdemann, K. Althoefer and A. Menciassi (2017), Highly dexterous 2-module soft robot for intra-organ navigation in minimally invasive surgery, **vol. 14**, no.1, pp. 1–9, ISSN 1478596X, doi:10.1002/rcs.1875.

Agarwal, G., N. Besuchet, B. Audergon and J. Paik (2016), Stretchable Materials for Robust Soft Actuators towards Assistive Wearable Devices, **vol. 6**, no.1, pp. 1–8, ISSN 20452322, doi:10.1038/srep34224.
www.nature.com/scientificreports

Ahmad, D., S. K. Sahu and K. Patra (2019), Fracture toughness, hysteresis and stretchability of dielectric elastomers under equibiaxial and biaxial loading, *Polymer Testing*, **vol. 79**, p. 106038, ISSN 01429418, doi:10.1016/j.polymertesting.2019.106038.

Antoniou, S. A., G. A. Antoniou, A. I. Antoniou and F. A. Granderath (2015), Past, present, and future of minimally invasive abdominal surgery, **vol. 19**, no.3, ISSN 19383797, doi:10.4293/JSLS.2015.00052.
http://www.ncbi.nlm.nih.gov/pubmed/26508823http://www.pubmedcentral.nih.gov/articlerender.fcgi?artid=PMC4589904

Atallah, S., B. Martin-Perez, D. Keller, J. Burke and L. Hunter (2015), Natural-orifice transluminal endoscopic surgery, **vol. 102**, no.2, pp. 73–92, ISSN 00071323, doi:10.1002/bjs.9710.
http://doi.wiley.com/10.1002/bjs.9710

Bishop-moser, J., G. Krishnan, C. Kim and S. Kota (2012), Design of Soft Robotic Actuators using Fluid-filled Fiber-Reinforced Elastomeric Enclosures in Parallel Combinations, *2012 IEEE/RSJ International Conference on Intelligent Robots and Systems*, pp. 4264–4269, doi:10.1109/IROS.2012.6385966.

Blanc, L., A. Delchambre and P. Lambert (2017), Flexible medical devices: Review of controllable stiffness solutions, **vol. 6**, no.3, pp. 1–31, ISSN 20760825, doi:10.3390/act6030023.

Boonvisut, P., R. Jackson and M. C. Çavuşoğlu (2012), Estimation of soft tissue mechanical parameters from robotic manipulation data, in *Proceedings - IEEE International Conference on Robotics and Automation*, volume 2012, Institute of Electrical and Electronics Engineers Inc., pp. 4667–4674, ISBN 9781467314039, ISSN 10504729, doi:10.1109/ICRA.2012.6225071.
/pmc/articles/PMC3966138/?report=abstracthttps://www.ncbi.nlm.nih.gov/pmc/articles/PMC3966138/

Cheng, S. S., Y. Kim and J. P. Desai (2017), Modeling and characterization of shape memory alloy springs with water cooling strategy in a neurosurgical robot, **vol. 28**, no.16, pp. 2167–2183, ISSN 15308138, doi:10.1177/1045389X16685443.

Cheng, S. S., Y. Kim and J. P. Desai (2018), Towards Real-Time SMA Control for a Neurosurgical Robot: MINIR-II, in *Robotics Research, Springer Proceedings in Advanced Robotics*, Eds. A. Bicchi and W. Burgard, Springer International Publishing, pp. 201–217, 2 edition, ISBN 9783319515328, doi:10.1007/978-3-319-51532-8.

Chou, C.-p. and B. Hannaford (1996), Measurement and Modelding of McKibben Pneumatic Artificial Muscles, **vol. 12**, no.1, pp. 90–102.

Cianchetti, M. and A. Menciassi (2017), Soft Robotics: Trends, Applications and Challenges, *Biosystems and Biorobotics*, **vol. 17**, pp. 75–85, ISSN 21953570, doi:10.1007/978-3-319-46460-2.
http://link.springer.com/10.1007/978-3-319-46460-2

Cianchetti, M., T. Ranzani, G. Gerboni, I. De Falco, C. Laschi and A. Menciassi (2013), STIFF-FLOP surgical manipulator: Mechanical design and experimental characterization of the single module, , no.August, pp. 3576–3581, ISSN 21530858, doi:10.1109/IROS.2013.6696866.

Clark, A. B. and N. Rojas (2019), Assessing the Performance of Variable Stiffness Continuum Structures of Large Diameter, **vol. 4**, no.3, pp. 2455–2462, ISSN 23773766, doi:10.1109/LRA.2019.2905980.

Gifari, M. W. (2018), Study on the Design of Soft Surgical Robots for Endoscopic NOTES Application.

Gifari, M. W., H. Naghibi, S. Stramigioli and M. Abayazid (2019), A review on recent advances in soft surgical robots for endoscopic applications, **vol. 15**, no.5, pp. 1–11, ISSN 1478596X, doi:10.1002/rcs.2010.

Henke, M. and G. Gerlach (2014), On a high-potential variable-stiffness device, **vol. 20**, no.4-5, pp. 599–606, ISSN 09467076, doi:10.1007/s00542-013-1995-5.

Hsu, Y. Y., K. Lucas, D. Davis, B. Elolampi, R. Ghaffari, C. Rafferty and K. Dowling (2013), Novel strain relief design for multilayer thin film stretchable interconnects, **vol. 60**, no.7, pp. 2338–2345, ISSN 00189383, doi:10.1109/TED.2013.2264217.

Irving, G., J. Teran and R. Fedkiw (2004), Invertible Finite Elements For Robust Simulation of Large Deformation, Technical report.

Jaeger, H. M. (2015), Celebrating Soft Matter's 10th Anniversary: Toward jamming by design, **vol. 11**, no.1, pp. 12–27, ISSN 17446848, doi:10.1039/c4sm01923g. www.rsc.org/softmatter

Kahi, C. J., P. Saxena and M. A. Khashab (2013), New Platforms and Devices in Colonoscopy, **vol. 42**, no.3, pp. 671–688.

Karimyan, V., M. Sodergren, J. Clark, G. Z. Yang and A. Darzi (2009), Navigation systems and platforms in natural orifice translumenal endoscopic surgery (NOTES), doi:10.1016/j.ijsu.2009.05.007.

Kim, Y., S. S. Cheng, M. Diakite, R. P. Gullapalli, J. M. Simard and J. P. Desai (2017), Toward the development of a flexible mesoscale MRI-compatible neurosurgical continuum robot, **vol. 33**, no.6, pp. 1386–1397, ISSN 15523098, doi:10.1109/TRO.2017.2719035.

Kim, Y. J., S. Cheng, S. Kim and K. Iagnemma (2013), A novel layer jamming mechanism with tunable stiffness capability for minimally invasive surgery, **vol. 29**, no.4, pp. 1031–1042, ISSN 15523098, doi:10.1109/TRO.2013.2256313.

Kohli, D. R. and J. Baillie (2019), How Endoscopes Work, in *Clinical Gastrointestinal Endoscopy*, Content Repository Only!, pp. 24–31, ISBN 9780323415095, doi:10.1016/B978-0-323-41509-5.00003-7. https://www.sciencedirect.com/science/article/pii/B9780323415095000037

Kurniawan, N. and M. Keuchel (2017), Flexible Gastro-intestinal Endoscopy — Clinical Challenges and Technical Achievements, doi:10.1016/j.csbj.2017.01.004.

Lenssen, J. (2019), Towards a steerable multi-module soft robotic endoscope for NOTES applications. https://essay.utwente.nl/78345/1/Lenssen{_}MA{_}EEMCS.pdf

Li, Z., R. Du, M. C. Lei and S. M. Yuan (2011), Design and analysis of a biomimetic wire-driven robot arm, in *ASME 2011 International Mechanical Engineering Congress and Exposition, IMECE 2011*, volume 7, pp. 191–198, ISBN 9780791854938, doi:10.1115/imece2011-63482.

Lin, Y. Y. (2019), Design of Pneumatic Soft Surgical Robot For Endoscopic NOTES and MIS Application with Reduced Size, Technical report, University of Twente.

Manti, M., V. Cacucciolo and M. Cianchetti (2016), Stiffening in soft robotics: A review of the state of the art, **vol. 23**, no.3, pp. 93–106, ISSN 10709932, doi:10.1109/MRA.2016.2582718.

Marchese, A. D., R. K. Katzschmann and D. Rus (2015), A recipe for soft fluidic elastomer robots, **vol. 2**, no.1, pp. 7–25, ISSN 21695172, doi:10.1089/soro.2014.0022.

McMahan, W., V. Chitrakaran, M. Csencsits, D. Dawson, I. D. Walker, B. A. Jones, M. Pritts, D. Dienno, M. Grissom and C. D. Rahn (2006), Field trials and testing of the OctArm continuum manipulator, **vol. 2006**, no.May, pp. 2336–2341, ISSN 10504729, doi:10.1109/ROBOT.2006.1642051.

Narang, Y. S., J. J. Vlassak and R. D. Howe (2018), Mechanically Versatile Soft Machines through Laminar Jamming, **vol. 28**, no.17, p. 1707136, ISSN 1616301X, doi:10.1002/adfm.201707136. http://doi.wiley.com/10.1002/adfm.201707136

Olympus (2019), EXTENDING THE ART OF SURGERY TO NEW DIMENSIONS. https://www.olympus-europa.com/medical/rmt/media/en/Content/Content-MSD/Documents/Brochures/VISERA-ELITE{_}ENDOEYE-FLEX-5{_}Brochure{_}4712.pdf

Olympus (2020), Endoscope Overview. https://www.olympus-europa.com/medical/en/Products-and-Solutions/Products/Gastroscopes.html

Peters, B. S., P. R. Armijo, C. Krause, S. A. Choudhury and D. Oleynikov (2018), Review of emerging surgical robotic technology, doi:10.1007/s00464-018-6079-2.

Polygerinos, P., N. Correll, S. A. Morin, B. Mosadegh, C. D. Onal, K. Petersen, M. Cianchetti, M. T. Tolley and R. F. Shepherd (2017), Soft Robotics: Review of Fluid-Driven Intrinsically Soft Devices; Manufacturing, Sensing, Control, and Applications in Human-Robot Interaction, **vol. 19**, no.12, ISSN 15272648, doi:10.1002/adem.201700016.

Popa, C., Z. Florin, N. Hajjar and O. Liviu (2018), Introduction in Laparoscopic Surgery : Concept and Devices, in *Laparoendoscopic S*, Ed. Florin Zaharie and Roxana Zaharie, Avid Science, chapter 1, pp. 2–25, ISBN 978-93-86337-62-7. https://www.avidscience.com/wp-content/uploads/2017/10/introduction-in-laparoscopic-surgery-concept-and-devices.pdf

Reilink, R. (2013), *Image-Based Robotic Steering of Advanced Flexible Endoscopes and Instruments*, Ph.D. thesis, University of Twente, doi:10.3990/1.9789036535267.

Robinson, T. N. and G. V. Stiegmann (2004), Minimally Invasive Surgery, **vol. 36**, no.1, pp. 48–51, doi:10.1055/s-2004-814113.

Runciman, M., A. Darzi and G. P. Mylonas (2019), Soft Robotics in Minimally Invasive Surgery, **vol. 6**, no.4, pp. 423–443, ISSN 21695180, doi:10.1089/soro.2018.0136.

Rus, D. and M. T. Tolley (2015), Design, fabrication and control of soft robots, **vol. 521**, no.7553, pp. 467–475, ISSN 14764687, doi:10.1038/nature14543.

Schneider, A. and H. Feussner (2017), Diagnostic Procedures, in *Biomedical Engineering in Gastrointestinal Surgery*, Elsevier, pp. 87–220, doi:10.1016/B978-0-12-803230-5.00005-1. https://linkinghub.elsevier.com/retrieve/pii/B9780128032305000051

Seah, T., T. N. Do, N. Takeshita, K. Y. Ho and S. J. Phee (2017), Future of Flexible Robotic Endoscopy Systems, Technical report.

Xin, H., J. S. Zelek and H. Carnahan (2006), Laparoscopic surgery, perceptual limitations and force: A review, , no.January, pp. 44–46.

Yeung, B. P. M. and T. Gourlay (2012), A technical review of flexible endoscopic multitasking platforms, **vol. 10**, no.7, pp. 345–354, ISSN 17439191, doi:10.1016/j.ijsu.2012.05.009. http://dx.doi.org/10.1016/j.ijsu.2012.05.009

Yeung, C. K., J. L. Cheung and B. Sreedhar (2019), Emerging next-generation robotic colonoscopy systems towards painless colonoscopy, **vol. 20**, no.4, pp. 196–205, ISSN 17512980, doi:10.1111/1751-2980.12718.
https://onlinelibrary.wiley.com/doi/abs/10.1111/1751-2980.12718